

## ABSTRACT

We propose a non-linear gravity inversion for simultaneously estimating the basement and Moho geometries, as well as the depth of the reference Moho along a profile crossing a passive rifted margin. We approximate the subsurface by an interpretation model composed of four layers. The shallowest represents water and has constant density contrast. The second has a number of sub-layers with constant density contrasts. The complexity of this layer depends on the available a priori information at the study area. The third layer represents the crust and has a predefined horizontal density variation along the profile. Finally, the deepest layer represents the mantle, with constant density contrast. Top and base of third layer represent the basement and Moho, respectively. The constant depth defining the base of the interpretation model defines the reference Moho. To obtain stable solutions, we impose smoothness on basement and Moho, force them to be close to previously estimated depths along the profile and also impose local isostatic equilibrium. Differently from previous methods, we introduce the information of local isostatic equilibrium by imposing smoothness on the lithostatic stress exerted at depth. Our method allows deviations from isostatic equilibrium along the profile, so that the interpreter can obtain a set of candidate models that fit the observed data and exhibit different degrees of isostatic equilibrium. Tests with synthetic data show the good performance of our method at regions with pronounced crustal thinning, which is typical of passive volcanic margins. Results obtained at the Pelotas basin, an example of passive volcanic margin at the southern of Brazil, agree with a previous interpretation obtained independently by using seismic data. These results show that, combined with a priori information, our method is a promising tool for interpreting gravity data on passive rifted margins.

## INTRODUCTION

Several methods have been proposed for using gravity data to estimate the boundaries of juxtaposed sedimentary layers, the relief of basement and the Mohorovicic discontinuity (or simply Moho). These geophysical discontinuities represent, in such methods, surfaces having density contrasts in subsurface. All these methods suffer from the inherent ambiguity (Skeels, 1947; Roy, 1962) in determining the true physical property distribution that produces a discrete set of observed gravity data. It is well known that, by using different density contrasts, it is possible to find different surfaces producing the same gravity data. To partially overcome this problem and obtain meaningful solutions, the interpreter must commonly use a priori information obtained from seismic data and/or boreholes in order to constrain the range of possible models. Here, we consider methods that approximate the subsurface by a set of layers that have constant or depth-dependent density contrasts and are separated by surfaces. These surfaces represent the geophysical discontinuities. In such methods, the geometry of the discontinuities are directly determined by estimating the geometrical parameters defining the surfaces.

Different criteria can be used to classify the methods that directly estimate the geometry of geophysical discontinuities. Those applied over a sedimentary basin, for example, can be considered local scale methods, whereas those applied over a continent or country can be considered regional scale methods and those applied over the whole globe can be considered global scale methods. They can also be classified according to the number of geophysical surfaces to be estimated. By using these criteria, it is possible to define a first group of methods estimating the geometry of a single surface. In this group, there are local scale methods in the space domain (e.g., Bott, 1960; Tanner, 1967; Cordell and Henderson,

1968; Dyrelus and Vogel, 1972; Pedersen, 1977; Richardson and MacInnes, 1989; Barbosa et al., 1997; Condi et al., 1999; Barbosa et al., 1999b,a; Silva et al., 2006; Chakravarthi and Sundararajan, 2007; Martins et al., 2010; Silva et al., 2010; Lima et al., 2011; Martins et al., 2011; Barnes and Barraud, 2012; Silva et al., 2014; Silva and Santos, 2017), and the Fourier domain (e.g., Oldenburg, 1974; Granser, 1987; Reamer and Ferguson, 1989; Guspí, 1993). Most of these methods were applied to estimate the relief of basement under a sedimentary basin. There are also regional scale methods for estimating a single surface representing the Moho in the space domain (e.g., Shin et al., 2009; Bagherbandi and Eshagh, 2012; Barzaghi and Biagi, 2014; Sampietro, 2015; Uieda and Barbosa, 2017) and in the Fourier domain (e.g., Braitenberg et al., 1997; Braitenberg and Zadro, 1999; van der Meijde et al., 2013). Additionally, there are some global scale methods, in space domain, for estimating the Moho (e.g., Sünkel, 1985; Sjöberg, 2009), and also the crustal thickness of the Moon (Zhang et al., 2019).

The second group of methods is formed by those estimating multiple surfaces separating layers with constant or depth-dependent density distribution (e.g., Condi et al., 1999; Camacho et al., 2011; Salem et al., 2014; Ferderer et al., 2017; García-Abdeslem, 2017; Salem, 2017). All these methods have been applied at local scale, to characterize a single sedimentary basin. It is known that these methods suffer from a greater ambiguity if compared with those estimating the geometry of a single surface. As a consequence, they require more a priori information to decrease the number of possible solutions. Some authors opted for combining gravity data with seismic and isostasy to reduce this inherent ambiguity and determine the geometries of basement and Moho surfaces. The geometry of these surfaces are important constraints on the amount of extension and heat flow at a margin during rifting (Watts and Fairhead, 1999; Gradmann et al., 2017).

Condi et al. (1999) proposed a non-linear gravity inversion for estimating the offshore deep structures of a rifted margin. They approximate the margin by using multiple irregular polygons, each having a uniform density and fixed horizontal position of their vertices. The polygons represent four homogeneous layers: water, sediments, crust and mantle. The parameters to be estimated are the constant densities of each polygon and the vertical positions of the vertices separating adjacent layers. The parameters are estimated by using a globally convergent Newton method together with an algorithm for solving sparse linear systems. Their method uses local isostasy and uniform extension for directly constraining the geometries of the shallow and deeper parts of their model, without necessarily forcing it to be in a perfect isostatic equilibrium.

Salem et al. (2014) presented a non-linear gravity inversion for estimating the surfaces representing basement and Moho on an onshore rifted basin. They approximate the rifted basin by using three homogeneous layers: sediments, crust and mantle. The layers are also described in terms of irregular polygons having constant density contrasts. The horizontal positions of the polygon vertices are fixed and the vertical positions of the vertices associated with basement and Moho are the parameters to be estimated by inversion. The position of the vertices associated with basement are estimated by using an iterative approach similar to that presented by Bott (1960) and Cordell and Henderson (1968). The difference is that, at each iteration, the Airy-Heiskanen model (Heiskanen and Moritz, 1967, p. 135) for local isostatic equilibrium is used to subsequently update the Moho geometry, forcing the model to be in perfect isostatic equilibrium according to the Airy-Heiskanen model. Notice that their method does not estimate the geometries of basement and Moho simultaneously. As properly pointed out by Silva et al. (2014), Bott's method does not define optimal step sizes at the iterative corrections, does not impose constraints for obtaining stable solutions, nor

use an objective stopping criterion. Consequently, the method presented by Salem et al. (2014) is also susceptible to these limitations.

García-Abdeslem (2017) presented a method for estimating the geometries of basement and Moho on the Montage Basin, located between Mexico and USA. He uses an approach based on flexural isostasy to estimate the Moho and compute a regional gravity field, which is subsequently subtracted from the observed gravity data to obtain a residual gravity field. His method consists in solving a non-linear inverse problem for estimating the basement geometry explaining the residual gravity field.

Salem (2017) presents a general framework for estimating the surfaces associated with basement and Moho on a rifted continental margin. He also approximates the margin by using a set of irregular polygons representing water, sediments, crust and mantle. The density contrasts of these layers are considered to be known functions of the horizontal position along the profile. His method is based on an empirical logistic function that acts as a gain control of the Moho uplift. Similarly to Salem et al. (2014) and García-Abdeslem (2017), the method presented by Salem (2017) does not estimate the surfaces of basement and Moho simultaneously. The Moho surface is estimated in a first step and then used to estimate the basement surface.

Ferderer et al. (2017) proposed a “general local isostasy” approach, which consists in combining the Airy-Heiskanen and Pratt-Hayford models (Heiskanen and Moritz, 1967) so that the crust density and geometry may vary laterally in order to maintain the local isostatic equilibrium on a profile crossing a rifted margin. Their approach also uses local isostasy to directly link the geometries of shallow and deeper structures with the purpose of reducing the range of possible solutions. They approximate the margin by using a set

stacked vertical prisms extending great distances in and out of the profile and propose a method for estimating their shapes and density contrasts by using a grid-search technique (Sen and Stoffa, 2013). Such techniques involve the systematic search for model parameters producing the best data fit and may be far from being practical in geophysical applications for the cases in which the model space is very large and the forward problem is slow.

We present a new local scale method for simultaneously estimating the geometries of basement and Moho surfaces, as well as a constant depth representing a reference Moho along a profile crossing a rifted margin. Our method is formulated, in the space domain, as a non-linear gravity inversion based on the Levenberg-Marquardt method (Silva et al., 2001; Aster et al., 2005), by following the same strategy of Barbosa et al. (1999b) to incorporate inequality constraints. The parameters to be estimated are the constant depth representing the reference Moho and the geometries of basement and Moho. At each iteration, our method simultaneously estimates corrections for the reference Moho, as well as the geometries of basement and Moho. In order to produce stable solutions, we use different constraints imposing smoothness on basement and Moho surfaces. Additionally, we force them to be close to some depths along the profile.

Similarly to Ferderer et al. (2017), we combine the Airy-Heiskanen and Pratt-Hayford models to impose local isostatic equilibrium. However, there are two significant differences between our *isostatic constraint* and those presented in earlier studies. The first one is the way we impose isostatic equilibrium. Differently from previous methods, we do not use local isostasy to directly link the geometries of basement and Moho. Rather, we impose smoothness on the lithostatic stress exerted by the interpretation model on a constant compensation depth, below which there are no lateral density variations. This information is directionally consistent with the basic principle of local isostatic equilibrium according to

the Airy-Heiskanen and Pratt-Hayford models. Our constraint introduces the information that the lithostatic stress must be mostly smooth along the entire profile, except at some isolated regions, where it can present abrupt variations. At these regions, our method enables the estimated model to deviate from the isostatic equilibrium. The second aspect by which our approach differs from those in the literature is that it allows the interpreter to control how much the estimated models can deviate from the isostatic equilibrium. As a consequence, the interpreter can obtain a set of candidate models that (i) fit the observed data and (ii) present different degrees of isostatic equilibrium.

Tests with synthetic data show the good performance of our method in simultaneously retrieving the geometry of basement and Moho of a simulated volcanic margin model. We also applied our method to invert gravity data on a profile over the Pelotas basin (Stica et al., 2014). This basin is located at the offshore southern of Brazil and is considered a classical example of volcanic passive margin (Geoffroy, 2005). We inverted gravity data provided by the combined global gravity field model EIGEN-6C4 (Förste et al., 2014), one of the latest releases of the “European Improved Gravity model of the Earth by New techniques” series. Our results are consistent with previous interpretations presented by Stica et al. (2014) and Zalán (2015), who combined seismic, gravity and magnetic data. These results show that, combined with a priori information, our method can be very effective in estimating a set of candidate models having different degrees of isostatic equilibrium at areas with abrupt crustal thinning, which is typically the case along volcanic passive margins.

## METHODOLOGY

### Forward problem

Let  $\mathbf{d}^o$  be the observed data vector, whose  $i$ -th element  $d_i^o$ ,  $i = 1, \dots, N$ , represents the observed gravity disturbance (Heiskanen and Moritz, 1967) at the point  $(x_i, y_i, z_i)$ , on a profile located over a rifted passive margin. The coordinates are referred to a topocentric Cartesian system, with  $z$ -axis pointing downward,  $y$ -axis along the profile and  $x$ -axis perpendicular to the profile. In local- and regional-scale studies, the gravity disturbance represents the vertical component of the gravitational attraction exerted by the gravity sources. It is more appropriated for geophysical applications, numerically similar to the classical free-air anomaly and uses the height relative to the reference ellipsoid (geometric height) instead of the Geoid (orthometric height) (Li and Götze, 2001; Fairhead et al., 2003; Hackney and Featherstone, 2003; Hinze et al., 2005; Vajda et al., 2006, 2007).

The density distribution in a rifted margin can be very complex. In volcanic margins, for example, the crust may consist partially or wholly of flood-basalts and tuffs, which are commonly imaged as Seaward Dipping Reflectors (SDR). Underneath this intruded crust, high-velocity seismic zones are usually interpreted as bodies of underplated mafic to ultra-mafic magma (Geoffroy, 2005). We assume that the actual mass distribution in a rifted passive margin can be schematically represented according to Figure 1. In this model, the subsurface is formed by four layers. Layer 1 is the shallowest and represents a water layer with constant density  $\rho^{(w)}$ . Layer 2 is formed by  $Q$  vertically adjacent sub-layers representing sediments, salt or volcanic rocks. In our example, this layer is formed by two sub-layers with constant densities  $\rho^{(q)}$ ,  $q = 1, 2$ . Different models can be created by changing the number  $Q$  according to the complexity of the study area and available a priori



information. In many cases, seismic data can be used to constrain the geometry of these shallow structures. Layer 3 represents the crust and we presume that its density  $\rho^c$  varies horizontally along the profile, according to a predefined function. In Figure 1, we consider that crust density assumes two possible values. It can be equal to  $\rho^{(cc)}$ , which represents the continental crust, or equal to  $\rho^{(oc)}$ , which represents the oceanic crust. However, more complex functions representing the crust density distribution can be specified according to interpreter's knowledge about the geology at study area. This approach presumes that bulk values can be used to approximate the real density distribution at the deeper parts of crust. Finally, Layer 4 represents a homogeneous mantle with constant density  $\rho^{(m)}$ . The surface separating the Layers 1 and 2 defines the basement relief whereas that separating Layers 3 and 4 defines the Moho. These surfaces are represented as dashed-white lines in Figure 1.

In order to define the anomalous mass distribution producing the observed gravity disturbance, we presume a reference mass distribution formed by two layers. The shallowest represents a homogeneous crust with constant density  $\rho^{(r)}$ . Its thickness is schematically represented in Figure 1. The deepest layer in the reference mass distribution represents a homogeneous mantle with constant density  $\rho^{(m)}$ . Notice that the mantle in the reference mass distribution has the same density as the mantle in our rifted margin model (Figure 1). The surface separating the crust and mantle in the reference mass distribution is conveniently called *reference Moho* (Figures 1 and 2). The reference model can be thought of as the outer layers of a concentric mass distribution producing the normal gravity field. In a local scale, this concentric mass distribution is close to a stack of two Bouguer slabs.

We consider that the anomalous mass distribution producing the observed data is defined as the difference between the rifted margin model and the reference mass distribution (Figure 1). As a consequence, the anomalous mass distribution is characterized by re-

gions with constant density contrasts. This anomalous distribution is approximated by an interpretation model formed by  $N$  columns of vertically stacked prisms (Figure 2). For convenience, we presume that there is an observed gravity disturbance over the center of each column. We consider that the prisms in the extremities of the interpretation model extend to infinity along the  $y$ -axis in order to prevent edge effects in the forward calculations. The  $i$ -th column is formed by vertically stacked prisms having infinite length along the  $x$ -axis and locally approximates the four layers of our rifted margin model (Figure 1).

Layer 1 is defined by a single prism, has thickness  $t_i^{(w)}$  and a constant density contrast  $\Delta\rho^{(w)} = \rho^{(w)} - \rho^{(r)}$ . Layer 2 is defined by the interpreter, according to the complexity of the study area and the available a priori information, by a set of  $Q$  vertically stacked prisms, each one with thickness  $t_i^{(q)}$  and constant density contrast  $\Delta\rho^{(q)} = \rho^{(q)} - \rho^{(r)}$ ,  $q = 1, \dots, Q$ . Layer 3 represents the deeper part of the crust, it is also formed by a single prism, has thickness  $t_i^{(c)}$  and density contrast  $\Delta\rho_i^{(c)} = \rho_i^{(c)} - \rho^{(r)}$ , with  $\rho_i^{(c)}$  being the crust density at the coordinate  $y_i$ ,  $i = 1, \dots, N$ , along the profile. According to Figure 2, the crust density contrast  $\Delta\rho_i^{(c)}$  may assume two possible values, depending on its position with respect to the  $y_{COT}$ . More complex models can be set by the interpreter according to the available a priori information at the study area. The top and bottom of this layer define, respectively, the basement and Moho. Finally, Layer 4 representing the mantle is divided into two sub-layers, each one formed by a single prism having the same constant density contrast  $\Delta\rho^{(m)} = \rho^{(m)} - \rho^{(r)}$ . The shallowest sub-layer has thickness  $t_i^{(m)}$ . Its top and bottom define, respectively, the depths of Moho and the compensation depth  $S_0$ . The deepest sub-layer has thickness  $\Delta S$ , top at  $S_0$  and bottom at  $S_0 + \Delta S$ , which defines the reference Moho.

Given the density contrasts, the COT position  $y_{COT}$ , the compensation depth  $S_0$ , the thickness  $t_i^{(w)}$  of the prisms defining Layer 1 and also the thickness  $t_i^{(q)}$ ,  $i = 1, \dots, N$ , of

the prisms forming the upper  $Q - 1$  sub-layers of Layer 2, it is possible to describe the interpretation model in terms of an  $M \times 1$  parameter vector  $\mathbf{p}$ ,  $M = 2N + 1$ , defined as follows:

$$\mathbf{p} = \begin{bmatrix} \mathbf{t}^Q \\ \mathbf{t}^m \\ \Delta S \end{bmatrix}, \quad (1)$$

where  $\mathbf{t}^Q$  and  $\mathbf{t}^m$  are  $N \times 1$  vectors whose  $i$ -th elements  $t_i^Q$  and  $t_i^m$  (Figure 2) represent the thickness of the prisms forming, respectively, the base of Layer 2 and the top of Layer 4. Notice that  $t_i^Q$  and  $t_i^m$ ,  $i = 1, \dots, N$ , approximate, respectively, the geometries of basement and Moho and  $\Delta S$  defines the depth of the reference Moho (Figure 2). In this case, the gravity disturbance produced by the interpretation model (the predicted gravity disturbance) at the position  $(x_i, y_i, z_i)$  can be written as the sum of the vertical component of the gravitational attraction exerted by the  $L$  prisms forming the interpretation model as follows:

$$d_i(\mathbf{p}) = k_g G \sum_{j=1}^L f_{ij}(\mathbf{p}), \quad (2)$$

where  $f_{ij}(\mathbf{p})$  represents an integral over the volume of the  $j$ -th prism. Here, these volume integrals are computed with the expressions proposed by Nagy et al. (2000), by using the open-source Python package *Fatiando a Terra* (Uieda et al., 2013).

## Inverse problem formulation

Let  $\mathbf{d}(\mathbf{p})$  be the predicted data vector, whose  $i$ -th element  $d_i(\mathbf{p})$  is the vertical component of the gravitational attraction (equation 2) exerted by the interpretation model at the position  $(x_i, y_i, z_i)$  on the profile. We estimate a particular parameter vector producing a predicted

data  $\mathbf{d}(\mathbf{p})$  as close as possible to the observed data  $\mathbf{d}^o$  by minimizing the goal function

$$\Gamma(\mathbf{p}) = \Phi(\mathbf{p}) + \sum_{\ell=0}^4 \mu_{\ell} \Psi_{\ell}(\mathbf{p}), \quad (3)$$

subject to the inequality constraint

$$p_j^{min} < p_j < p_j^{max}, \quad j = 1, \dots, M, \quad (4)$$

where  $p_j^{min}$  and  $p_j^{max}$  define, respectively, lower and upper bounds for the  $j$ -th element of  $\mathbf{p}$ .

In equation 3,  $\mu_{\ell}$  is the weight assigned to the  $\ell$ -th regularizing function  $\Psi_{\ell}(\mathbf{p})$ ,  $\ell = 0, \dots, 4$ , and  $\Phi(\mathbf{p})$  is the misfit function given by

$$\Phi(\mathbf{p}) = \frac{1}{N} \|\mathbf{d}^o - \mathbf{d}(\mathbf{p})\|_2^2, \quad (5)$$

where  $\|\cdot\|_2^2$  represents the squared Euclidean norm. Notice that our method estimates the parameter vector  $\mathbf{p}$  (equation 1), which contains the geometries of basement and Moho, as well as the thickness  $\Delta S$  defining the depth of the reference Moho (Figure 2). The geometries of Layer 1 and of the upper sub-layers forming Layer 2, as well as the compensation depth  $S_0$  (Figure 2) are predefined by using the bathymetry and the available a priori information. These predefined quantities remain fixed during the inversion. Details about the regularizing functions  $\Psi_{\ell}(\mathbf{p})$ ,  $\ell = 0, \dots, 4$  and the numerical procedure to solve this non-linear inverse problem are given in the following sections.

### Isostatic constraint

Consider that no vertical forces are acting on the lateral surfaces of each column forming the model (Figure 2). In this case, the lithostatic stress (pressure) exerted by the  $i$ -th column at the surface  $S_0$  can be computed according to the Archimedes' principle as follows:

$$t_i^{(w)} \rho^{(w)} + t_i^{(1)} \rho_i^{(1)} + \dots + t_i^{(Q)} \rho_i^{(Q)} + t_i^{(c)} \rho_i^{(c)} + t_i^{(m)} \rho^{(m)} = \tau_i, \quad (6)$$

where  $\tau_i$  is the ratio of lithostatic stress to the mean gravity value on the study area. By rearranging terms in equation 6 and using the relation

$$S_0 = t_i^{(w)} + t_i^{(1)} + \dots + t_i^{(Q)} + t_i^{(c)} + t_i^{(m)}, \quad (7)$$

it is possible to show that:

$$\Delta\tilde{\rho}_i^{(Q)} t_i^{(Q)} + \Delta\tilde{\rho}_i^{(m)} t_i^{(m)} + \Delta\tilde{\rho}_i^{(w)} t_i^{(w)} + \Delta\tilde{\rho}_i^{(1)} t_i^{(1)} + \dots + \Delta\tilde{\rho}_i^{(Q-1)} t_i^{(Q-1)} + \rho_i^{(c)} S_0 = \tau_i, \quad (8)$$

where  $\Delta\tilde{\rho}_i^{(\alpha)} = \rho_i^{(\alpha)} - \rho_i^{(c)}$ ,  $\alpha = w, 1, \dots, Q-1, Q, m$ . In order to describe the lithostatic stress exerted by all columns forming the interpretation model on the surface  $S_0$ , equation 8 can be written as follows:

$$\mathbf{M}^{(Q)}\mathbf{t}^{(Q)} + \mathbf{M}^{(m)}\mathbf{t}^{(m)} + \mathbf{M}^{(w)}\mathbf{t}^{(w)} + \mathbf{M}^{(1)}\mathbf{t}^{(1)} + \dots + \mathbf{M}^{(Q-1)}\mathbf{t}^{(Q-1)} + \boldsymbol{\rho}^{(c)}S_0 = \boldsymbol{\tau}, \quad (9)$$

where  $\boldsymbol{\tau}$  is an  $N \times 1$  vector whose  $i$ -th element is the  $\tau_i$  (equation 6) associated with the  $i$ -th column;  $\mathbf{t}^{(\alpha)}$ ,  $\alpha = w, 1, \dots, Q-1, Q, m$ , is an  $N \times 1$  vector with  $i$ -th element defined by the thickness  $t_i^{(\alpha)}$  of a prism in the  $i$ -th column;  $\mathbf{M}^{(\alpha)}$  is an  $N \times N$  diagonal matrix whose elements are defined by the density contrasts  $\Delta\tilde{\rho}_i^{(\alpha)}$ ,  $i = 1, \dots, N$ , of the prisms in a layer and  $\boldsymbol{\rho}^{(c)}$  is an  $N \times 1$  vector containing the densities of the prisms representing the crust.

Let us now use an approach similar to that presented by Ferderer et al. (2017) to combine the Airy-Heiskanen and Pratt-Hayford models (Heiskanen and Moritz, 1967) in order to impose local isostatic equilibrium. We impose this condition by varying both density and geometry of the crust along the rifted margin. In this case, the lithostatic stress exerted by the interpretation model must be constant at the compensation depth  $S_0$  (Figure 2). Differently from previous approaches in literature, we impose isostatic equilibrium by forcing the lithostatic stress to be smooth at  $S_0$ . We apply the first-order Tikhonov regularization

(Aster et al., 2005) to the vector  $\boldsymbol{\tau}$  (equation 9), obtaining the following expression:

$$\mathbf{R}(\mathbf{C}\mathbf{p} + \mathbf{D}\mathbf{t}) = \mathbf{0}, \quad (10)$$

where  $\mathbf{0}$  is a vector with null elements and the remaining terms are given by:

$$\mathbf{C} = \begin{bmatrix} \mathbf{M}^{(Q)} & \mathbf{M}^{(m)} & \mathbf{0} \end{bmatrix}_{N \times M}, \quad (11)$$

$$\mathbf{D} = \begin{bmatrix} \mathbf{M}^{(w)} & \mathbf{M}^{(1)} & \dots & \mathbf{M}^{(Q-1)} & \boldsymbol{\rho}^{(c)} \end{bmatrix}_{N \times (QN+1)}, \quad (12)$$

$$\mathbf{t} = \begin{bmatrix} \mathbf{t}^{(w)} \\ \mathbf{t}^{(1)} \\ \vdots \\ \mathbf{t}^{(Q-1)} \\ S_0 \end{bmatrix}_{(QN+1) \times 1}, \quad (13)$$

and  $\mathbf{R}$  is an  $(N-1) \times N$  matrix, whose element  $ij$  is defined as follows:

$$[\mathbf{R}]_{ij} = \begin{cases} 1 & , \quad j = i \\ -1 & , \quad j = i + 1 \\ 0 & , \quad \text{otherwise} \end{cases}. \quad (14)$$

Finally, from equation 10, it is possible to define the regularizing function  $\Psi_0(\mathbf{p})$  (equation 3):

$$\Psi_0(\mathbf{p}) = \|\mathbf{W}\mathbf{R}(\mathbf{C}\mathbf{p} + \mathbf{D}\mathbf{t})\|_2^2, \quad (15)$$

where  $\mathbf{W}$  is an  $(N-1) \times (N-1)$  diagonal matrix having constant elements  $0 < w_{ii} \leq 1$ ,  $i = 1, \dots, N-1$ . Function  $\Psi_0(\mathbf{p})$  defines the *Isostatic constraint*.

Notice that, by minimizing the function  $\Psi_0(\mathbf{p})$  (equation 15), the method imposes smoothness on the lithostatic stress exerted by the interpretation model on the compensation depth  $S_0$ . Matrix  $\mathbf{W}$  controls the relative amount of isostatic equilibrium imposed

along the profile. In the particular case in which all diagonal elements  $w_{ii}$  have the same constant value, the same amount of isostatic equilibrium is imposed along the whole profile. On the other hand, different amounts of isostatic equilibrium can be imposed along the profile by varying the values of these elements. Elements  $w_{ii} \approx 1$  impose a smooth lithostatic stress curve at the transition between columns  $i$  and  $i + 1$  of the interpretation model. Elements  $w_{ii} \approx 0$  allow abrupt variations in the lithostatic stress curve between columns  $i$  and  $i + 1$  of the interpretation model. By using all elements  $w_{ii} = 1$ , we impose full isostatic equilibrium along the entire profile. Alternatively, we may enable the interpretation model to deviate from the isostatic equilibrium by conveniently decreasing the numerical values assigned to the elements  $w_{ii}$  at specific regions along the profile. The strategy used to define the elements  $w_{ii}$  is presented in the specific section describing the computational procedures for solving the inverse problem.

### Smoothness constraints

These constraints impose smoothness on the adjacent thickness of the prisms defining the geometries of basement (base of Layer 2) and Moho (top of Layer 4). This information is introduced by applying the first-order Tikhonov regularization (Aster et al., 2005) to the vectors  $\mathbf{t}^{(Q)}$  and  $\mathbf{t}^{(m)}$  (equation 1). Mathematically, these constraints are represented by the regularizing functions  $\Psi_1(\mathbf{p})$  and  $\Psi_2(\mathbf{p})$  (equation 3):

$$\Psi_1(\mathbf{p}) = \|\mathbf{S}\mathbf{p}\|_2^2 \quad (16)$$

and

$$\Psi_2(\mathbf{p}) = \|\mathbf{T}\mathbf{p}\|_2^2, \quad (17)$$

where  $\mathbf{S}$  and  $\mathbf{T}$  are matrices given by:

$$\mathbf{S} = \begin{bmatrix} \mathbf{R} & \mathbf{0} & \mathbf{0} \end{bmatrix}_{(N-1) \times M} \quad (18)$$

and

$$\mathbf{T} = \begin{bmatrix} \mathbf{0} & \mathbf{R} & \mathbf{0} \end{bmatrix}_{(N-1) \times M} . \quad (19)$$

In these equations,  $\mathbf{R}$  is defined by equation 14 and  $\mathbf{0}$  are matrices with all elements equal to zero.

## Equality constraints

In order to incorporate a priori information at isolated points on the basement and Moho surfaces, we use an approach similar to those proposed by Barbosa et al. (1997) and Barbosa et al. (1999a).

### *Equality constraint on vector $\mathbf{t}^Q$*

Let  $\mathbf{a}$  be a vector whose  $k$ -th element  $a_k$ ,  $k = 1, \dots, A$ , is the difference between a known basement depth and the sum of the thickness of the upper parts of the interpretation model (water layer and the upper sub-layers of Layer 2), all at the same horizontal coordinate  $y_k^A$  of the profile. These differences, which must be positive, are used to define the regularizing function  $\Psi_2(\mathbf{p})$  (equation 3):

$$\Psi_2(\mathbf{p}) = \|\mathbf{A}\mathbf{p} - \mathbf{a}\|_2^2, \quad (20)$$

where  $\mathbf{A}$  is an  $A \times M$  matrix whose  $k$ -th line has one element equal to one and all the remaining elements equal to zero. The location of the single non-null element in the  $k$ -th line of  $\mathbf{A}$  depends on the coordinate  $y_k^A$  of the known thickness  $a_k$ . Let us consider,



for example, an interpretation model formed by  $N = 10$  columns. Consider also that the thickness of the deepest sub-layer of Layer 2 at the coordinates  $y_1^A = y_4$  and  $y_2^A = y_9$  are equal to 25 and 35.7 km, respectively. In this case,  $A = 2$ ,  $\mathbf{a}$  is a  $2 \times 1$  vector with elements  $a_1 = 25$  and  $a_2 = 35.7$  and  $\mathbf{A}$  is a  $2 \times M$  matrix ( $M = 2N + 1 = 21$ ). The element 4 of the first line and the element 9 of the second line of  $\mathbf{A}$  are equal to 1 and all its remaining elements are equal to zero.

#### *Equality constraint on vector $\mathbf{t}^m$*

Let  $\mathbf{b}$  be a vector whose  $k$ -th element  $b_k$ ,  $k = 1, \dots, B$ , is the difference between the compensation depth  $S_0$  and the known Moho depth at the horizontal coordinate  $y_k^B$  of the profile. These differences, which must be positive, define known thickness values of the upper part of Layer 4. These values are used to define the regularizing function  $\Psi_3(\mathbf{p})$  (equation 3):

$$\Psi_3(\mathbf{p}) = \|\mathbf{B}\mathbf{p} - \mathbf{b}\|_2^2, \quad (21)$$

where  $\mathbf{B}$  is a  $B \times M$  matrix whose  $k$ -th line has one element equal to one and all the remaining elements equal to zero. This matrix is defined in the same way as matrix  $\mathbf{A}$  (equation 20).

### **Computational procedures for solving of the inverse problem**

The parameter vector  $\mathbf{p}$  (equation 1) minimizing the goal function  $\Gamma(\mathbf{p})$  (equation 3), subjected to the inequality constraint (equation 4), is estimated in three steps (Step 1, Step 2 and Step 3 described in the following subsections). At each step, the goal function is minimized by using the Levenberg-Marquardt method (Silva et al., 2001; Aster et al., 2005) and

the inequality constraint (equation 4) is incorporated by using the same strategy employed by Barbosa et al. (1999b). All derivatives of the misfit function  $\Phi(\mathbf{p})$  (equation 5) with respect to the parameters are computed by using a finite difference approximation.

*Considerations about the weights  $\mu_0, \mu_1, \mu_2, \mu_3$  and  $\mu_4$*

An important aspect of our method is related to the values attributed to the weights  $\mu_\ell$  (equation 3). Their values can be very dependent on the particular characteristics of the interpretation model and there is no analytical rule to define them. To overcome this problem, we normalize the  $\mu_\ell$  values as follows:

$$\mu_\ell = \tilde{\mu}_\ell \frac{E_\Phi}{E_\ell}, \quad \ell = 0, \dots, 4, \quad (22)$$

where  $\tilde{\mu}_\ell$  is a positive scalar and  $E_\Phi/E_\ell$  is a normalizing constant. In this equation,  $E_\ell$  represents the median of the elements forming the main diagonal of the Hessian matrix of the  $\ell$ -th constraining function  $\Psi_\ell(\mathbf{p})$  (equations 15, 16, 17, 20 and 21). The constant  $E_\Phi$  is defined in a similar way by using the Hessian matrix of the misfit function  $\Phi(\mathbf{p})$  (equation 5) computed with the initial approximation  $\mathbf{p}^{(0)}$  for the parameter vector  $\mathbf{p}$  (equation 1) at the Step 1 (described in the following subsection). According to this empirical strategy, the weights  $\mu_\ell$  are defined by using the positive scalars  $\tilde{\mu}_\ell$  (equation 22), which are less dependent on the particular characteristics of the interpretation model.

*Step 1*

This step is represented in blue at the flow diagram shown in Figure 3. It consists in solving the inverse problem without imposing the isostatic constraint, by using  $\tilde{\mu}_0 = 0$  (equation 22). At this step, the interpreter must set:

- Parameters defining the interpretation model (Figure 2): density contrasts  $\Delta\rho^{(\alpha)}$ ,  $\alpha = w, 1, \dots, Q, cc, oc, m$ , COT position  $y_{COT}$ , thickness  $t_i^{(w)}$  of the prisms defining Layer 1, thickness  $t_i^{(q)}$ ,  $i = 1 \dots, N$ , of the prisms forming the upper  $Q - 1$  sub-layers of Layer 2 and isostatic compensation depth  $S_0$ . Figure 2 illustrates the case in which the second layer is formed by  $Q = 2$  parts. This number, however, can be changed according to the study area.
- Parameters for the inversion: weights  $\tilde{\mu}_\ell$ ,  $\ell = 1, \dots, 4$  (equation 22), associated to the smoothness and equality constraints (equations 16, 17, 20 and 21), lower and upper bounds  $p_j^{min}$  and  $p_j^{max}$  (equation 4),  $j = 1, \dots, M$ , for the parameters to be estimated, vectors  $\mathbf{a}$  (equation 20) and  $\mathbf{b}$  (equation 21) containing known thickness values and an initial approximation  $\mathbf{p}^{(0)}$  for the parameter vector  $\mathbf{p}$  (equation 1). The initial approximation  $\mathbf{p}^{(0)}$  must satisfy the inequality constraints (equation 4).

The initial approximation  $\mathbf{p}^{(0)}$  is used to compute the Hessian matrix of the misfit function  $\Phi(\mathbf{p})$  (equation 5), which is subsequently used to compute the constant  $E_\Phi$  (equation 22). The estimated parameter vector obtained at the end of Step 1 is conveniently called  $\mathbf{p}^{(1)}$ . The main goal in this step is finding suitable values for the parameters defining the interpretation model and those used for inversion. Several trials may be necessary to find suitable values for these parameters.

### *Step 2*

Step 2 is represented in red at the flow diagram (Figure 3) and consists in obtaining an estimated parameter vector  $\mathbf{p}^{(2)}$  by imposing full isostatic equilibrium on the interpretation model along the entire profile. In this step, the interpreter must use the same initial

approximation  $\mathbf{p}^{(0)}$  of Step 1. Additionally, the interpreter must set the matrix  $\mathbf{W}$  equal to the identity and find a suitable value for the weight  $\tilde{\mu}_0$  (equation 22) controlling the isostatic constraint (equation 15). We presume that, by imposing full isostatic equilibrium along the entire profile, the estimated parameter vector  $\mathbf{p}^{(2)}$  will produce a mostly good data fit, except at some isolated regions. We assume that, at these regions, the passive margin deviates from the local isostatic equilibrium.

### *Step 3*

Step 3 represented in green at the flow diagram (Figure 3). It consists in using  $\mathbf{p}^{(2)}$  as initial approximation to obtain an estimated parameter vector  $\mathbf{p}^{(3)}$  by imposing different amounts of isostatic equilibrium on the interpretation model along the profile. At this step, the interpreter must compute the diagonal elements  $w_{ii}$  of the matrix  $\mathbf{W}$  (equation 15) in order to enable the interpretation model to deviate from isostatic equilibrium in the regions presenting large residuals. The elements of  $\mathbf{W}$  are computed as follows:

$$w_{ii} = \exp \left[ -\frac{\left( r_i^{(2)} + r_{i+1}^{(2)} \right)^2}{4\sigma} \right], \quad (23)$$

where  $\sigma$  is a positive constant,  $\mathbf{p}^{(2)}$  is the estimated parameter vector obtained in the previous step and the variables  $r_i^{(2)} = d_i^o - d_i(\mathbf{p}^{(2)})$  and  $r_{i+1}^{(2)} = d_{i+1}^o - d_{i+1}(\mathbf{p}^{(2)})$  represent, respectively, the residuals between observed and predicted data (equation 2) at the positions  $(x_i, y_i, z_i)$  and  $(x_{i+1}, y_{i+1}, z_{i+1})$ . Notice that equation 23 defines elements  $w_{ii}$  in the interval  $]0, 1]$ . Additionally, this equation results in  $w_{ii} \approx 1$  at regions where the residuals are close to zero and  $w_{ii} \approx 0$  at regions presenting large residuals. The positive constant  $\sigma$  controls the deviation from isostatic equilibrium. Small  $\sigma$  values allow large deviations from isostatic equilibrium, resulting in estimated models close to that obtained at Step 1. Large  $\sigma$  values

allow small deviations from isostatic equilibrium, resulting in estimated models close to that obtained at Step 2. This strategy to define the elements of matrix  $\mathbf{W}$  (equation 15) presumes that the isostatic constraint may produce large residuals at some regions along the profile. To counteract this problem, our method enables the interpretation model to deviate from isostatic equilibrium at these regions. This idea is in agreement with the fact that isostatic equilibrium at passive rifted margin cannot be totally explained by local models.

### *Practical considerations*

Our algorithm depends on several parameters that significantly impact the estimated models and cannot be automatically set without the interpreters judgment. They are the parameters  $\tilde{\mu}_1$ ,  $\tilde{\mu}_2$ ,  $\tilde{\mu}_3$  and  $\tilde{\mu}_4$  (Step 1),  $\tilde{\mu}_0$  (Step 2) and  $\sigma$  (Step 3). Based on our practical experience, we suggest some empirical procedures for setting these parameters at each step. They are schematically represented at the flow diagram (Figure 3).

At Step 1, set  $\tilde{\mu}_1 = \tilde{\mu}_2 = 0$  and try different positive values for  $\tilde{\mu}_3$  and  $\tilde{\mu}_4$ . These two parameters control the equality constraints (equations 20 and 21) imposing a priori information at isolated points on the basement and Moho surfaces. Good guesses are, respectively,  $10^1$  and  $10^2$ . Normally,  $\tilde{\mu}_4$  is one order of magnitude greater than  $\tilde{\mu}_3$ . The parameters  $\tilde{\mu}_3$  and  $\tilde{\mu}_4$  must be the smallest positive numbers resulting in an estimated model  $\mathbf{p}'$  with basement and Moho surfaces close to the values provided by the a priori information at some isolated points. Notice that  $\mathbf{p}'$  is an intermediate model obtained by using only the equality constraints. Consequently, there must be some pinnacles in the estimated models, around the points associated with the a priori information. This effect has already been observed by Barbosa et al. (1997). The acceptability criterion described

above to define the values of  $\tilde{\mu}_3$  and  $\tilde{\mu}_4$  is represented by the decision point  $D(\tilde{\mu}_3, \tilde{\mu}_4)$  at the flow diagram (Figure 3).

By using the chosen values for  $\tilde{\mu}_3$  and  $\tilde{\mu}_4$ , try different positive values for  $\tilde{\mu}_1$  and  $\tilde{\mu}_2$ . These parameters control the smoothness of basement and Moho surfaces (equations 16 and 17). Usually,  $\tilde{\mu}_2$  is one order of magnitude greater than  $\tilde{\mu}_1$ . Good guesses are  $10^1$  and  $10^2$ . These parameters must be the smallest positive numbers producing an estimated model satisfying the following conditions: (i) the data fit must be good along the entire profile and (ii) the pinnacles must be completely removed or attenuated as much as possible. This acceptability criterion to define the values of  $\tilde{\mu}_1$  and  $\tilde{\mu}_2$  is represented by the decision point  $D(\tilde{\mu}_1, \tilde{\mu}_2)$  at the flow diagram (Figure 3).

At Step 2, try different positive values for  $\tilde{\mu}_0$  (equation 22). This parameter controls the smoothness of the lithostatic stress exerted by the interpretation model at the compensation depth  $S_0$ . Generally,  $\tilde{\mu}_0$  is one or two orders of magnitude greater than  $\tilde{\mu}_1$ . Good guesses are  $10^2$  or  $10^3$ . Large values produce a poor data fit along the profile. This parameter must be the largest positive number resulting in an estimated model satisfying two conditions: (i) the lithostatic stress curve must be smooth along the entire profile and (ii) there must be a good data fit along the entire profile, except at some isolated regions that can show relatively large residuals. This acceptability criterion for the value of  $\tilde{\mu}_0$  is represented by the decision point  $D(\tilde{\mu}_0)$  at the flow diagram (Figure 3).

Finally, at Step 3, try different positive values for  $\sigma$  (equation 23). This parameter controls the deviations of the interpretation model from the isostatic equilibrium at regions presenting large residuals. Small values produce estimated models close to that obtained at Step 1. On the other hand, large values produce estimated models close to that obtained

at Step 2. This parameter must be set as the largest positive number producing (i) a good data-fit along the entire profile and (ii) an estimated model different from those obtained at Steps 1 and 2. This acceptability criterion to define the value of  $\sigma$  is represented by the decision point  $D(\sigma)$  at the flow diagram (Figure 3). A good practice is to generate a set of estimates by using different values for  $\sigma$ .

## APPLICATIONS TO SYNTHETIC DATA

We have simulated a simple volcanic margin model formed by four layers: water, sediments + seaward dipping reflectors, crust (continental and oceanic) and mantle. Parameters defining this model are shown in Table 1. The density values of our model are compatible with those commonly used in literature (e.g., Gradmann et al., 2017). By following the algorithm described in the previous section, we inverted the synthetic gravity disturbance data produced by our volcanic margin model.

Figure 4 shows the results obtained at Step 1 of our algorithm. The interpretation model was defined by using the parameters shown in Table 1. The parameters  $\tilde{\mu}_1$ ,  $\tilde{\mu}_2$  and  $\tilde{\mu}_3$  (equation 22) used at Step 1 have values  $10^1$ ,  $10^1$  and  $10^2$ , respectively. Remember that this estimate was obtained without imposing the isostatic constraint, by using  $\tilde{\mu}_0 = 0$ . We assumed  $S_0 = 41$  km and chose an initial approximation for  $\Delta S$  equal to 8.5 km, which corresponds to a reference Moho deeper than the true one (Table 1). Notice that, not only the initial approximation for the reference Moho, but also those used for basement and Moho surfaces (dashed blue lines) are very different from the true model (continuous black lines). As we can see in Figure 4, the estimated Moho and reference Moho are very close to the true ones. On the other hand, the estimated basement is very smooth and present large differences relative to the true one. Despite these large differences, the predicted gravity

disturbance and lithostatic stress are very close to the simulated values. In this example, the small density contrast at basement relative to that at Moho forces the Moho to play a dominant role in fitting the lithostatic stress curve and the simulated gravity data.

Figure 5 shows the estimated model obtained at the end of Step 2, by using  $\tilde{\mu}_0 = 10^2$  (equation 22). In comparison to the estimated model obtained at Step 1 (Figure 4), this result shows a very smooth lithostatic stress curve as a consequence of the isostatic constraint. The use of the isostatic constraint has produced little effect on the estimated reference Moho and resulted in a relatively worse estimated Moho. On the other hand, it reduced the large differences between the estimated and true basement surfaces. The main improvement occurs along the first  $\approx 100$  km on the profile, where the true model exhibits a pronounced crustal thinning. The region between 100 and 200 km, however, shows large differences between the estimated and true basement. At this region, we can also notice the presence of large differences between the simulated and predicted gravity disturbances.

Figures ??, ?? and ?? show estimated models obtained at the Step 3 of our algorithm by using different values for the parameter  $\sigma$  (equation 23). In comparison with the estimated model obtained at Step 2 (Figure 5), the new models show better data fits and improved estimates for Moho and reference Moho. All models show a small artifact at the estimated Moho at the position  $y \approx 150$  km, which shows the large residuals between the predicted and simulated gravity data in Figure 5. This artifact is a consequence of the small density contrast associated to basement. This small density contrast forces the Moho to play a dominant role in the inversion. Notice that the lithostatic stress curves in all these new models reflect, predominantly, the geometry of the estimated Moho and are less sensitive to the geometry of basement. In this case, the small density contrast associated to basement causes our method to concentrate changes in the Moho surface at the region located between



100 and 200 km to improve the data fit. It is worth noting that, at this region, the new lithostatic stress curves contain abrupt variations and the estimated models deviate from the isostatic equilibrium.

The main differences between the models shown in Figures ??, ?? and ?? occur at basement, along the first 200 km of the profile. According to the practical considerations explained in the previous section, we consider that the estimated model shown in Figure ??, with  $\sigma = 22$ , is the best. Data fit is very good along the entire profile, the estimated Moho and reference Moho are very close to the true ones and the estimated basement is intermediate between those obtained at Steps 1 and 2 (Figures 4 and 5). Notice that the estimated model obtained with the smallest  $\sigma$  (Figure ??) is close the that obtained at Step 1 (Figure 4). In this case, the predicted lithostatic stress curve is less smooth than that produced by the best model. On the other hand, the estimated model obtained with the largest  $\sigma$  (Figure ??) is close that obtained at Step 2 (Figure 5). In this case, the predicted lithostatic stress curve is smoother than that produced by the best model.

Figure ?? shows an alternative model obtained at Step 3. The density values in Layer 2 (sediment + SDR) used to obtain this model are different from those of the true model (Table 1). The corresponding estimated model obtained at Step 1 is not shown and that obtained at Step 2 is represented by the dashed blue lines in Figure ?. Notice that, in this case, the absolute value of the absolute density contrast associated to basement is greater than that used to generate the estimated models shown in Figures ??, ?? and ?. As we can see, the artifact shown in the estimated Moho, at the position  $y \approx 150$  km, is considerably smaller in the alternative model than in the previous ones (Figures ??, ?? and ?). This result confirms that the artifact shown in the estimated Moho of the previous models is a consequence of the small density contrast associated to basement. Besides, this result

shows that our method can produce good estimates of the basement and Moho surfaces, even by using approximated values for the density contrasts at Layer 2. Additional results illustrating the sensitivities of our method to different combinations of constraints, different initial approximations and errors in the density of Layer 2 (sediment + SDR) are available as supplementary material at xxxxxxxxxx. **(Note to reviewers: the online repository will be made public upon publication)**

## APPLICATION TO REAL DATA

We applied our method to invert the gravity disturbance data on a profile located over the Pelotas basin (Stica et al., 2014), southern of Brazil (Figure 9). This basin is considered a classical example of volcanic margin (Geoffroy, 2005). The gravity disturbance data are provided by the combined global gravity field model EIGEN-6C4 (Förste et al., 2014), one of the latest releases of the “European Improved Gravity model of the Earth by New techniques” series. We have used data from ETOPO-1 to constraint the bathymetry along the profile (Amante and Eakins, 2009). Additionally, we have used a priori information about the basement and Moho depths obtained from the seismic interpretations presented by Stica et al. (2014) and Zalán (2015) to define the equality constraints (equations 20 and 21) and the initial approximation used in the non-linear inversion.

Figure 10 shows the estimated model obtained at Step 2, by using  $(\tilde{\mu}_0, \tilde{\mu}_1, \tilde{\mu}_2, \tilde{\mu}_3) = (10^2, 10^1, 10^1, 10^2)$  (equation 22). Parameters defining the interpretation model are the same used to define our synthetic volcanic margin (Table 1). As we can see, the estimated model produces a good data fit along the whole profile, except at region  $\approx 150$  km.

Figures 11, 12 and 13 show estimated models obtained at Step 3 by using different

values for the parameter  $\sigma$  (equation 23). Differently from the model obtained at Step 2 (Figure 10), the new models show better data fits along the entire profile. The estimated lithostatic stress curves produced by these estimated models show abrupt variations at an isolated region close to 150 km and is very smooth on the remaining parts of the profile. These results suggest that the margin is mostly in isostatic equilibrium, except at the region  $\approx 150$ . Notice that the estimated models shown in Figures 11, 12 and 13 exhibit a feature very similar to that artifact obtained with synthetic data (Figures ??, ?? and ??). Based on those results with synthetic data, we consider that this feature is an artifact produced by the small density contrast at basement. Figure 14 shows an alternative model obtained at Step 3. The density values in Layer 2 (sediment + SDR) used to obtain this model are different from those of the true model (Table 1). The corresponding estimated model obtained at Step 1 is not shown and that obtained at Step 2 is represented by the dashed blue lines.

The estimated models shown in Figures 11 and 14 are close to that proposed independently by Zalán (2015) (continuous black lines), by interpreting seismic data. The larger differences ( $\approx 10$  km) occur at the basement, along the first 100 km of the profile. At this region, Zalán proposes a steep variation in basement relief, which shows a maximum depth  $\approx 30$  km. Despite these large differences, our estimated models produce a very good data fit at this region. It means that, the steep variation proposed by Zalán in the basement relief cannot be determined by using only gravity data. It is worth stressing that our results were obtained by using gravity data provided by the global gravity model EIGEN6C4 (Förste et al., 2014), whereas Zalán (2015) obtained his result by combining gravity, magnetic and seismic sections available to the petroleum industry. Despite these differences, our results are very consistent with that presented independently by Zalán (2015). Additional

results for the Pelotas basin are available as supplementary material at xxxxxxxx. (**Note to reviewers: the online repository will be made public upon publication**)

## CONCLUSIONS

We present a new gravity inversion method for simultaneously estimating the geometries of basement and Moho, as well as the constant depth of the reference Moho on a profile crossing a passive rifted margin. The method is formulated as a non-linear inverse problem by imposing local isostatic equilibrium. The parameters to be estimated by inversion define the geometries of basement and Moho, as well as a constant depth defining the reference Moho.

There are two main differences between our method and those in the literature. The first is that, at each iteration of the non-linear inversion at each step, our method estimates corrections for the geometries of basement and Moho simultaneously. It means that we do not estimate the Moho, use it to compute a residual gravity anomaly and then invert these residual data to obtain the basement. Another difference is that we do not use local isostasy to directly link the geometries of basement and Moho. Rather, we impose smoothness on the lithostatic stress exerted by the interpretation model on a constant compensation depth, below which there is no lateral density variations.

Tests with synthetic data show that our method can be used to generate a set of possible solutions with different “degrees of isostatic equilibrium”. The interpreter must choose the “best estimated model” based on the available priori information and its knowledge about the study area. Our results show the robustness of our method to the initial approximation used in the non-linear inversion. Besides, show that the isostatic constraint can

considerably improve the estimated models at regions showing pronounced crustal thinning, which are typical of volcanic passive margins. Applications to real data over the Pelotas basin, considered a classical volcanic margin at the southern of Brazil, produced results in agreement with a previous interpretation obtained independently. These results show that, combined with priori information, our method can be a useful tool for interpreting gravity data on rifted margins. Additional results with synthetic and real data are available as supplementary material at xxxxxxxx. **(Note to reviewers: the online repository will be made public upon publication)**

The problem of simultaneously estimating the geometries of basement and Moho surfaces is very ambiguous and some simplifications must be made. One of these simplifications consists in considering bulk density values for each column forming the continental and oceanic crusts. The interpreter must predefine the function describing the horizontal density variation of the crust along the profile, including the region close the COT. In most practical situations, however, the interpreter will not have access to a detailed description of the density variations within the crust and a regional approximation will have to be used instead. As a consequence, local errors in the estimated basement and Moho surfaces are expected at regions presenting local density variations in the deeper parts of continental crust and in the oceanic crust. Another limitation of our method is that it requires a priori information about the upper layers located below the water layer. This information can be obtained, for example, from seismic data and be used to set the densities of the layers located right below the ocean bottom. If no a priori information is available at the study area, the interpreter will have to use approximated values and test different models. Errors in this approximation may negatively impact the estimated model, especially in the basement surface. Further research could be conducted to generalize our method to estimate three dimensional models

and also include lateral density variations in the mantle.

## **ACKNOWLEDGMENTS**

## REFERENCES

- Amante, C., and B. Eakins, 2009, Etopo1 1 arc-minute global relief model: Procedures, data sources and analysis.
- Aster, R. C., B. Borchers, and C. H. Thurber, 2005, Parameter estimation and inverse problems (international geophysics): Academic Press.
- Bagherbandi, M., and M. Eshagh, 2012, Crustal thickness recovery using an isostatic model and goce data: *Earth, Planets and Space*, **64**, 1053–1057.
- Barbosa, V. C. F., J. ao B. C. Silva, and W. E. Medeiros, 1997, Gravity inversion of basement relief using approximate equality constraints on depths: *Geophysics*, **62**, 1745–1757.
- Barbosa, V. C. F., J. B. C. Silva, and W. E. Medeiros, 1999a, Gravity inversion of a discontinuous relief stabilized by weighted smoothness constraints on depth: *GEOPHYSICS*, **64**, 1429–1437.
- , 1999b, Stable inversion of gravity anomalies of sedimentary basins with nonsmooth basement reliefs and arbitrary density contrast variations: *GEOPHYSICS*, **64**, 754–764.
- Barnes, G., and J. Barraud, 2012, Imaging geologic surfaces by inverting gravity gradient data with depth horizons: *Geophysics*, **77**, G1–G11.
- Barzaghi, R., and L. Biagi, 2014, The collocation approach to Moho estimate: *Annals of Geophysics*.
- Bott, M. H. P., 1960, The use of rapid digital computing methods for direct gravity interpretation of sedimentary basins: *Geophysical Journal International*, **3**, 63–67.
- Braitenberg, C., F. Pettenati, and M. Zadro, 1997, Spectral and classical methods in the evaluation of moho undulations from gravity data: The ne italian alps and isostasy: *Journal of Geodynamics*, **23**, 5 – 22.
- Braitenberg, C., and M. Zadro, 1999, Iterative 3d gravity inversion with integration of

- seismologic data: *Bollettino di Geofisica Teorica ed Applicata*, **40**, 469–475.
- Camacho, A. G., J. Fernández, and J. Gottsmann, 2011, A new gravity inversion method for multiple subhorizontal discontinuity interfaces and shallow basins: *Journal of Geophysical Research: Solid Earth*, **116**.
- Chakravarthi, V., and N. Sundararajan, 2007, 3d gravity inversion of basement relief a depth-dependent density approach: *GEOPHYSICS*, **72**, I23–I32.
- Condi, F. J., C. A. Zelt, D. S. Sawyer, and G. J. Hirasaki, 1999, Gravity inversion for rifted margin deep structure using extension and isostatic constraints: *Geophysical Journal International*, **138**, 435–446.
- Cordell, L., and R. G. Henderson, 1968, Iterative three-dimensional solution of gravity anomaly data using a digital computer: *GEOPHYSICS*, **33**, 596–601.
- Dyrelus, D., and A. Vogel, 1972, Improvement of convergency in iterative gravity interpretation: *Geophysical Journal of the Royal Astronomical Society*, **27**, 195–205.
- Fairhead, J. D., C. M. Green, and D. Blitzkow, 2003, The use of gps in gravity surveys: *The Leading Edge*, **22**, 954–959.
- Ferderer, R., J. Mariano, and J. Shoffner, 2017, Inversion of gravity data using general local isostasy: 87th Annual International Meeting, SEG, Expanded Abstracts, 1718–1722.
- Förste, C., S. Bruinsma, O. Abrikosov, J.-M. Lemoine, J. C. Marty, F. Flechtner, G. Balmino, F. Barthelmes, and R. Biancale, 2014, EIGEN-6C4 The latest combined global gravity field model including GOCE data up to degree and order 2190 of GFZ Potsdam and GRGS Toulouse: <https://doi.org/10.5880/icgem.2015.1>.
- García-Abdeslem, J., 2017, Nonlinear inversion of isostatic residual gravity data from montage basin, northern gulf of california: *GEOPHYSICS*, **82**, G45–G55.
- Geoffroy, L., 2005, Volcanic passive margins: *Comptes Rendus Geoscience*, **337**, 1395 –



1408.

- Gradmann, S., C. Haase, and J. Ebbing, 2017, Isostasy as a tool to validate interpretations of regional geophysical datasets – application to the mid-norwegian continental margin: Geological Society, London, Special Publications, **447**, 279–297.
- Granser, H., 1987, Three-dimensional interpretation of gravity data from sedimentary basins using an exponential density-depth function: *Geophysical Prospecting*, **35**, 1030–1041.
- Guspi, F., 1993, Noniterative nonlinear gravity inversion: *Geophysics*, **58**, 935–940.
- Hackney, R. I., and W. E. Featherstone, 2003, Geodetic versus geophysical perspectives of the gravity anomaly: *Geophysical Journal International*, **154**, 35–43.
- Heiskanen, W. A., and H. Moritz, 1967, *Physical geodesy*: W.H. Freeman and Company.
- Hinze, W. J., C. Aiken, J. Brozena, B. Coakley, D. Dater, G. Flanagan, R. Forsberg, T. Hildenbrand, G. R. Keller, J. Kellogg, R. Kucks, X. Li, A. Mainville, R. Morin, M. Pilkington, D. Plouff, D. Ravat, D. Roman, J. Urrutia-Fucugauchi, M. Véronneau, M. Webring, and D. Winester, 2005, New standards for reducing gravity data: The north american gravity database: *Geophysics*, **70**, J25–J32.
- Li, X., and H.-J. Götze, 2001, Ellipsoid, geoid, gravity, geodesy, and geophysics: *Geophysics*, **66**, 1660–1668.
- Lima, W. A., C. M. Martins, J. B. Silva, and V. C. Barbosa, 2011, Total variation regularization for depth-to-basement estimate: Part 2 physicogeologic meaning and comparisons with previous inversion methods: *Geophysics*, **76**, I13–I20.
- Martins, C. M., V. C. Barbosa, and J. B. Silva, 2010, Simultaneous 3d depth-to-basement and density-contrast estimates using gravity data and depth control at few points: *GEOPHYSICS*, **75**, I21–I28.
- Martins, C. M., W. A. Lima, V. C. Barbosa, and J. B. Silva, 2011, Total variation regular-

- ization for depth-to-basement estimate: Part 1 - mathematical details and applications: Geophysics, **76**, I1–I12.
- Nagy, D., G. Papp, and J. Benedek, 2000, The gravitational potential and its derivatives for the prism: Journal of Geodesy, **74**, 311–326.
- Oldenburg, D. W., 1974, The inversion and interpretation of gravity anomalies: Geophysics, **39**, 526–536.
- Pedersen, L. B., 1977, Interpretation of potential field data a generalized inverse approach: Geophysical Prospecting, **25**, 199–230.
- Reamer, S. K., and J. F. Ferguson, 1989, Regularized twodimensional fourier gravity inversion method with application to the silent canyon caldera, nevada: Geophysics, **54**, 486–496.
- Richardson, R. M., and S. C. MacInnes, 1989, The inversion of gravity data into three-dimensional polyhedral models: Journal of Geophysical Research: Solid Earth, **94**, 7555–7562.
- Roy, A., 1962, Ambiguity in geophysical interpretation: Geophysics, **27**, 90–99.
- Salem, A., 2017, Gravity modeling a rifted continental margin.
- Salem, A., C. Green, M. Stewart, and D. D. Lerma, 2014, Inversion of gravity data with isostatic constraints: GEOPHYSICS, **79**, A45–A50.
- Sampietro, D., 2015, Geological units and moho depth determination in the western balkans exploiting goce data: Geophysical Journal International, **202**, 1054–1063.
- Sen, M. K., and P. L. Stoffa, 2013, Global optimization methods in geophysical inversion, second edition ed.: Cambridge University Press.
- Shin, Y. H., C.-K. Shum, C. Braitenberg, S. M. Lee, H. Xu, K. S. Choi, J. H. Baek, and J. U. Park, 2009, Three-dimensional fold structure of the tibetan moho from grace gravity

- data: Geophysical Research Letters, **36**.
- Silva, J. B., D. C. Costa, and V. C. Barbosa, 2006, Gravity inversion of basement relief and estimation of density contrast variation with depth: GEOPHYSICS, **71**, J51–J58.
- Silva, J. B., A. S. Oliveira, and V. C. Barbosa, 2010, Gravity inversion of 2d basement relief using entropic regularization: Geophysics, **75**, I29–I35.
- Silva, J. B. C., W. E. Medeiros, and V. C. F. Barbosa, 2001, Pitfalls in nonlinear inversion: pure and applied geophysics, **158**, 945–964.
- Silva, J. B. C., and D. F. Santos, 2017, Efficient gravity inversion of basement relief using a versatile modeling algorithm: GEOPHYSICS, **82**, G23–G34.
- Silva, J. B. C., D. F. Santos, and K. P. Gomes, 2014, Fast gravity inversion of basement relief: Geophysics, **79**, G79–G91.
- Sjöberg, L. E., 2009, Solving vening meinesz-moritz inverse problem in isostasy: Geophysical Journal International, **179**, 1527–1536.
- Skeels, D. C., 1947, Ambiguity in gravity interpretation: Geophysics, **12**, 43–56.
- Stica, J. M., P. V. Zalán, and A. L. Ferrari, 2014, The evolution of rifting on the volcanic margin of the pelotas basin and the contextualization of the paranetendeka lip in the separation of gondwana in the south atlantic: Marine and Petroleum Geology, **50**, 1 – 21.
- Sünkel, H., 1985, An isostatic Earth model: Scientific report 367, Department of Geodetic Science and Surveying, The Ohio State University, Columbus, Ohio.
- Tanner, J. G., 1967, An automated method of gravity interpretation: Geophysical Journal of the Royal Astronomical Society, **13**, 339–347.
- Uieda, L., and V. C. Barbosa, 2017, Fast nonlinear gravity inversion in spherical coordinates with application to the south american moho: Geophysical Journal International, **208**,

162–176.

Uieda, L., V. C. Oliveira Jr., and V. C. F. Barbosa, 2013, Modeling the earth with fatiando a terra: Proceedings of the 12th Python in Science Conference, 96 – 103.

Vajda, P., P. Vaníček, and B. Meurers, 2006, A new physical foundation for anomalous gravity: *Studia Geophysica et Geodaetica*, **50**, 189–216.

Vajda, P., P. Vaníček, P. Novák, R. Tenzer, and A. Ellmann, 2007, Secondary indirect effects in gravity anomaly data inversion or interpretation: *Journal of Geophysical Research: Solid Earth*, **112**.

van der Meijde, M., J. Julià, and M. Assumpção, 2013, Gravity derived moho for south america: *Tectonophysics*, **609**, 456 – 467. (Moho: 100 years after Andrija Mohorovicic).

Watts, A. B., and J. D. Fairhead, 1999, A processoriented approach to modeling the gravity signature of continental margins: *The Leading Edge*, **18**, 258–263.

Zalán, P. V., 2015, Similarities and differences between magma-poor and volcanic passive margins applications to the brazilian marginal basins: 14th International Congress of the Brazilian Geophysical Society & EXPOGEF, Rio de Janeiro, Brazil, 3-6 August 2015, 37–42.

Zhang, Y., W. D. Mooney, C. Chen, and J. Du, 2019, Interface inversion of gravitational data using spherical triangular tessellation: An application for the estimation of the moon’s crustal thickness: *Geophysical Journal International*, ggz026.

## LIST OF TABLES

1 Properties of the synthetic margin model. The model extends from  $y = 0$  km to  $y = 380$  km, the Continent-Ocean Transition (COT) is located at  $y_{COT} = 165$  km and the reference Moho is located at 53 km (Figures 1 and 2). The density contrasts  $\Delta\rho^{(\alpha)} = \rho^{(\alpha)} - \rho^{(r)}$  were defined by using the reference value  $\rho^{(r)} = 2850$  kg/m<sup>3</sup>, which coincides with the density  $\rho^{(cc)}$  attributed to the continental crust.

2 Properties attributed for the Pelotas volcanic margin. The interpretation model extends from  $y = 0$  km to  $y = 383$  km, the Continent-Ocean Transition (COT) is located at  $y_{COT} = 350$  km and the reference Moho is located at 43 200 km (Figures 1 and 2). The density contrasts  $\Delta\rho^{(\alpha)} = \rho^{(\alpha)} - \rho^{(r)}$  were defined by using the reference value  $\rho^{(r)} = 2870$  kg/m<sup>3</sup>, which coincides with the density  $\rho^{(cc)}$  attributed to the continental crust.

## LIST OF FIGURES

1     Rifted margin model formed by four layers. Layer 1 represents a water with constant density  $\rho^{(w)}$ . Layer 2 is split into  $Q$  sub-layers according to the complexity of the study area. In this example,  $Q = 2$ . These sub-layers represent sediments, salt or volcanic rocks and have constant densities  $\rho^{(q)}$ ,  $q = 1, \dots, Q$ . Layer 3 represents the crust. In this example, its density  $\rho(c)$  assumes two possible values  $\rho^{(cc)}$  and  $\rho^{(oc)}$  representing, respectively, continental and oceanic crust. More complex models can be generated by using a function describing the lateral density variations within the crust. Finally, Layer 4 represents a homogeneous mantle with constant density  $\rho^{(m)}$ . Basement, Moho and reference Moho are represented by the dashed-white lines. The reference mass distribution is formed by an upper layer with constant density  $\rho^{(r)}$  and base at the reference Moho. Below this layer, we presume a reference distribution with the same constant density  $\rho^{(m)}$  of the mantle.

2     Interpretation model formed by  $N$  columns of vertically stacked prisms. Each column is formed by four layers of prisms and locally approximates the rifted margin model shown in Figure 1. Layer 2 is formed by  $Q$  sub-layers according to the complexity of the study area. In this example,  $Q = 2$ . The thickness  $t_i^Q$  and  $t_i^m$  of the prisms forming, respectively, the base of Layer 2 and the top of Layer 4 at the  $i$ -column are indicated. Each prism has a constant density contrast defined as the difference between its corresponding density at the rifted margin model and the constant density  $\rho^{(r)}$  of the shallowest layer forming the reference density distribution (Figure 1). Basement, Moho and the reference Moho are represented by dashed-white lines. The continuous black line represents the compensation depth at  $S_0$ . The reference Moho is located at  $S_0 + \Delta S$ .

3     Flow diagram of the algorithm. Steps 1, 2 and 3 are represented in blue, red and green, respectively. Decision points are represented by diamonds. The parallelograms

represent input parameters. The remaining processes of the algorithm are represented by rectangles. For convenience, we omitted some input parameters related to the interpretation model and the inversion (see the subsection *Step 1*). Details about this flow diagram are explained at subsection **Computational procedures for solving of the inverse problem**.

4 Application to synthetic data. Results obtained at Step 1. (Bottom panel) True and estimated surfaces, initial basement and Moho used in the inversion (initial guess) and a priori information at some points on basement and Moho (known depths). (Middle panel) True and predicted lithostatic stress curves computed by using equation 6. The values are multiplied by a constant gravity value equal to  $9.81 \text{ m/s}^2$ . (Upper panel) Gravity disturbance data produced by the volcanic margin model (simulated data), by the estimated model (predicted data) and by the initial guess (initial guess data). Parameters  $\tilde{\mu}_1$ ,  $\tilde{\mu}_2$  and  $\tilde{\mu}_3$  (equation 22) have values  $10^1$ ,  $10^1$  and  $10^2$ , respectively,  $S_0 = 48 \text{ km}$  and the density contrasts are those shown in Table 1.

5 Application to synthetic data. Results obtained at Step 2 by using  $\tilde{\mu}_0 = 10^3$  (equation 22). The remaining informations are the same shown in the caption of Figure 4.

6 Application to synthetic data. Results obtained at Step 3 by using the estimated model shown in Figure 5 as initial approximation (dashed blue lines) and  $\sigma = 11$  (equation 23). The remaining informations are the same shown in the caption of Figure 4.

7 Application to synthetic data. Results obtained at Step 3 by using the estimated model shown in Figure 5 as initial approximation (dashed blue lines) and  $\sigma = 1$  (equation 23). The remaining informations are the same shown in the caption of Figure 4.

8 Application to synthetic data. Results obtained at Step 3 by using the estimated model shown in Figure 5 as initial approximation (dashed blue lines) and  $\sigma = 18$  (equa-

tion 23). The remaining informations are the same shown in the caption of Figure 4.

9 Application to real data on Pelotas basin, Brazil. Gravity disturbance provided by the global gravity field model EIGEN-6C4 (Förste et al., 2014) at the study area. The black straight line indicates the gravity profile over the Pelotas basin. The end points of the profile have coordinates (geodetic latitude and longitude)  $(-27.72, -48.23)$  and  $(-29.66, -44.94)$ . The coordinates are referred to the WGS84 datum.

10 Application to real data on Pelotas basin, Brazil. Results obtained at Step 2. (Bottom panel) Estimated surfaces, initial basement and Moho used in the inversion (initial guess) and a priori information at some points on basement and Moho (known depths). The continuous black lines represent a previous interpretation presented by Zalán (2015) at the same study area. (Middle panel) Estimated lithostatic stress curve computed by using equation 6. The values are multiplied by  $9.81 \text{ m/s}^2$ . (Upper panel) Observed gravity disturbance, data produced by the estimated model (predicted data) and data produced by the initial approximation (initial guess data). We used  $(\tilde{\mu}_0, \tilde{\mu}_1, \tilde{\mu}_2, \tilde{\mu}_3) = (10^2, 10^1, 10^1, 10^2)$  (equation 22),  $S_0 = 41 \text{ km}$ , density contrasts equal to those shown in Table 1 and initial approximation for  $\Delta S$  equal to 1 km.

11 Application to real data on Pelotas basin, Brazil. Results obtained at Step 3 by using the estimated model shown in Figure 10 as initial approximation (dashed blue lines) and  $\sigma = 58$  (equation 23). The remaining informations are the same shown in the caption of Figure 10.

12 Application to real data on Pelotas basin, Brazil. Results obtained at Step 3 by using the estimated model shown in Figure 10 as initial approximation (dashed blue lines) and  $\sigma = 40$  (equation 23). The remaining informations are the same shown in the caption of Figure 10.



13 Application to real data on Pelotas basin, Brazil. Results obtained at Step 3 by using the estimated model shown in Figure 10 as initial approximation (dashed blue lines) and  $\sigma = 63$  (equation 23). The remaining informations are the same shown in the caption of Figure 10.

14 Application to real data on Pelotas basin, Brazil. Results obtained at Step 3 by using density values  $\rho^{(1)}$  (sediment) and  $\rho^{(2)}$  (SDR) different from those defined in Table 1. This estimated model was obtained by using  $\sigma = 17$  (equation 23). The dashed blue lines (initial guess surfaces) represent the corresponding model obtained at Step 2 (not shown). The remaining informations are the same shown in the caption of Figure 10.

<b>Geological meaning</b>	$\rho^{(\alpha)}$ (kg/m <sup>3</sup> )	$\Delta\rho^{(\alpha)}$ (kg/m <sup>3</sup> )	$\alpha$
water	1030	−1820	<i>w</i>
sediments	2600	−250	1
continental crust	2850	0	<i>cc</i>
oceanic crust	2885	35	<i>oc</i>
mantle	3250	400	<i>m</i>

Table 1: Properties of the synthetic margin model. The model extends from  $y = 0$  km to  $y = 380$  km, the Continent-Ocean Transition (COT) is located at  $y_{COT} = 165$  km and the reference Moho is located at 53 km (Figures 1 and 2). The density contrasts  $\Delta\rho^{(\alpha)} = \rho^{(\alpha)} - \rho^{(r)}$  were defined by using the reference value  $\rho^{(r)} = 2850$  kg/m<sup>3</sup>, which coincides with the density  $\rho^{(cc)}$  attributed to the continental crust.

<b>Geological meaning</b>	$\rho^{(\alpha)}$ (kg/m <sup>3</sup> )	$\Delta\rho^{(\alpha)}$ (kg/m <sup>3</sup> )	$\alpha$
water	1030	−1840	<i>w</i>
sediments	2350	−520	1
SDR	2855	−15	2
continental crust	2870	0	<i>cc</i>
oceanic crust	2885	15	<i>oc</i>
mantle	3240	370	<i>m</i>

Table 2: Properties attributed for the Pelotas volcanic margin. The interpretation model extends from  $y = 0$  km to  $y = 383$  km, the Continent-Ocean Transition (COT) is located at  $y_{COT} = 350$  km and the reference Moho is located at 43 200 km (Figures 1 and 2). The density contrasts  $\Delta\rho^{(\alpha)} = \rho^{(\alpha)} - \rho^{(r)}$  were defined by using the reference value  $\rho^{(r)} = 2870$  kg/m<sup>3</sup>, which coincides with the density  $\rho^{(cc)}$  attributed to the continental crust.

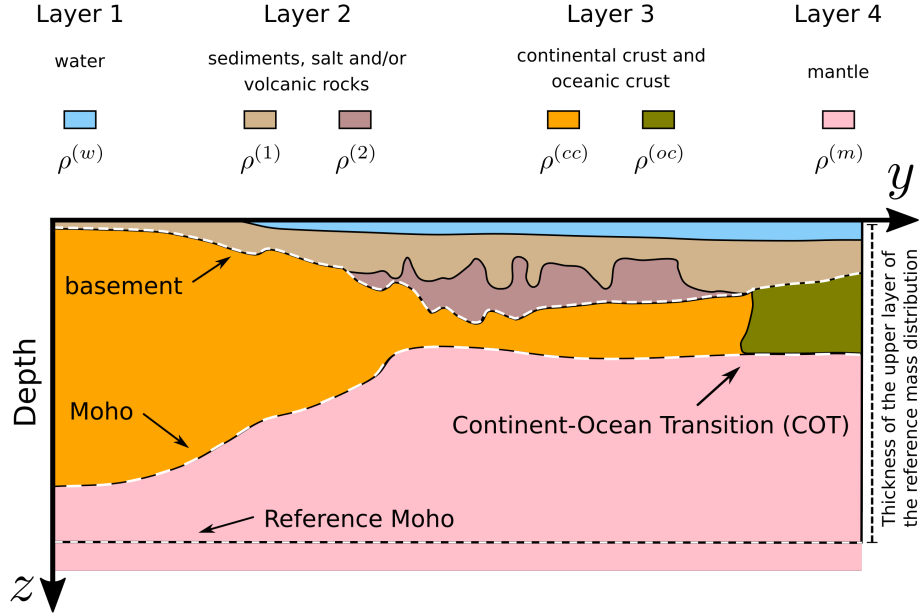


Figure 1: Rifted margin model formed by four layers. Layer 1 represents a water with constant density  $\rho^{(w)}$ . Layer 2 is split into  $Q$  sub-layers according to the complexity of the study area. In this example,  $Q = 2$ . These sub-layers represent sediments, salt or volcanic rocks and have constant densities  $\rho^{(q)}$ ,  $q = 1, \dots, Q$ . Layer 3 represents the crust. In this example, its density  $\rho(c)$  assumes two possible values  $\rho^{(cc)}$  and  $\rho^{(oc)}$  representing, respectively, continental and oceanic crust. More complex models can be generated by using a function describing the lateral density variations within the crust. Finally, Layer 4 represents a homogeneous mantle with constant density  $\rho^{(m)}$ . Basement, Moho and reference Moho are represented by the dashed-white lines. The reference mass distribution is formed by an upper layer with constant density  $\rho^{(r)}$  and base at the reference Moho. Below this layer, we presume a reference distribution with the same constant density  $\rho^{(m)}$  of the mantle.

– GEO-XXXX

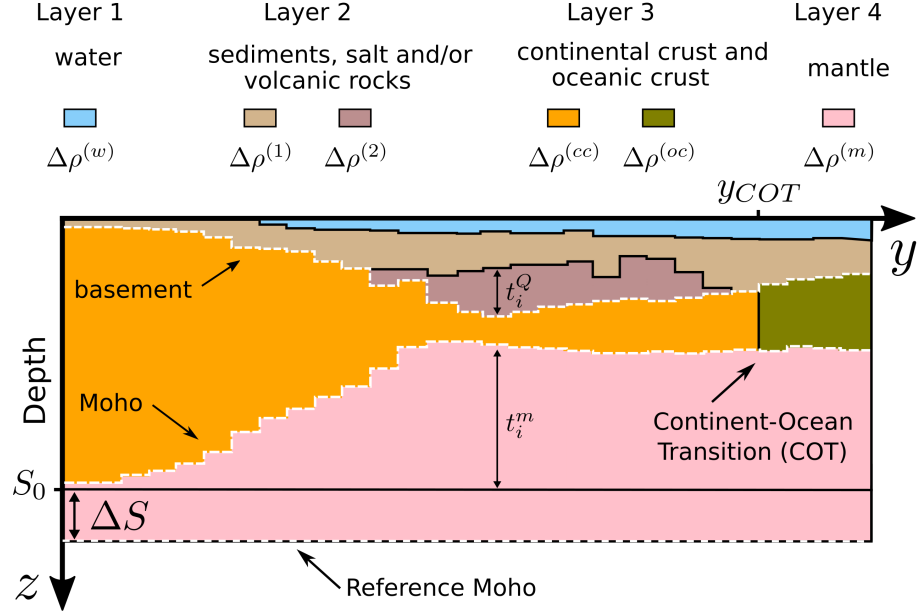


Figure 2: Interpretation model formed by  $N$  columns of vertically stacked prisms. Each column is formed by four layers of prisms and locally approximates the rifted margin model shown in Figure 1. Layer 2 is formed by  $Q$  sub-layers according to the complexity of the study area. In this example,  $Q = 2$ . The thickness  $t_i^Q$  and  $t_i^m$  of the prisms forming, respectively, the base of Layer 2 and the top of Layer 4 at the  $i$ -column are indicated. Each prism has a constant density contrast defined as the difference between its corresponding density at the rifted margin model and the constant density  $\rho^{(r)}$  of the shallowest layer forming the reference density distribution (Figure 1). Basement, Moho and the reference Moho are represented by dashed-white lines. The continuous black line represents the compensation depth at  $S_0$ . The reference Moho is located at  $S_0 + \Delta S$ .

– GEO-XXXX

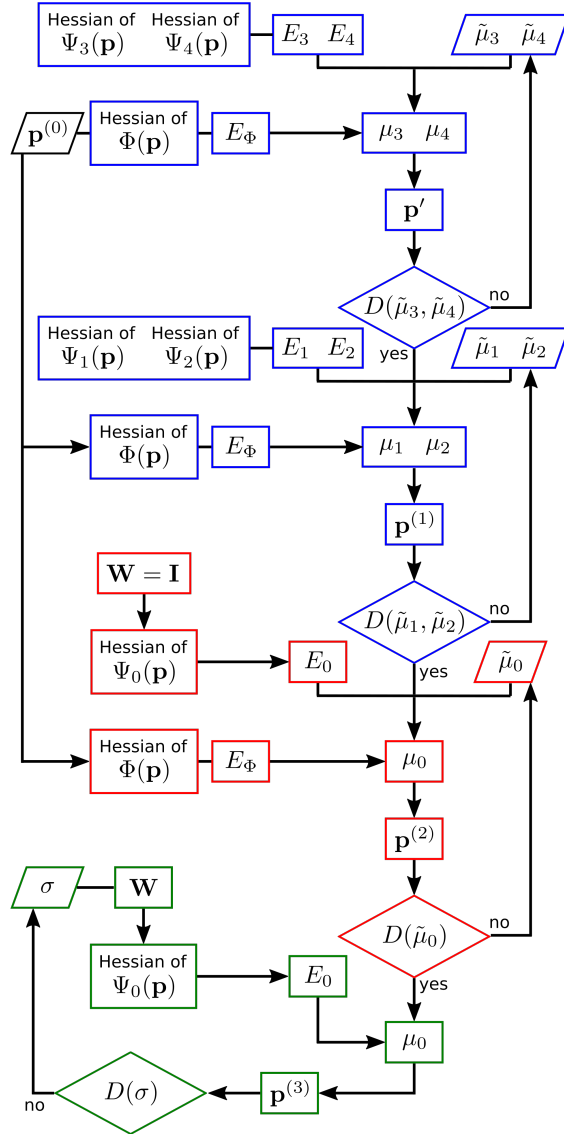


Figure 3: Flow diagram of the algorithm. Steps 1, 2 and 3 are represented in blue, red and green, respectively. Decision points are represented by diamonds. The parallelograms represent input parameters. The remaining processes of the algorithm are represented by rectangles. For convenience, we omitted some input parameters related to the interpretation model and the inversion (see the subsection *Step 1*). Details about this flow diagram are explained at subsection **Computational procedures for solving of the inverse problem**.

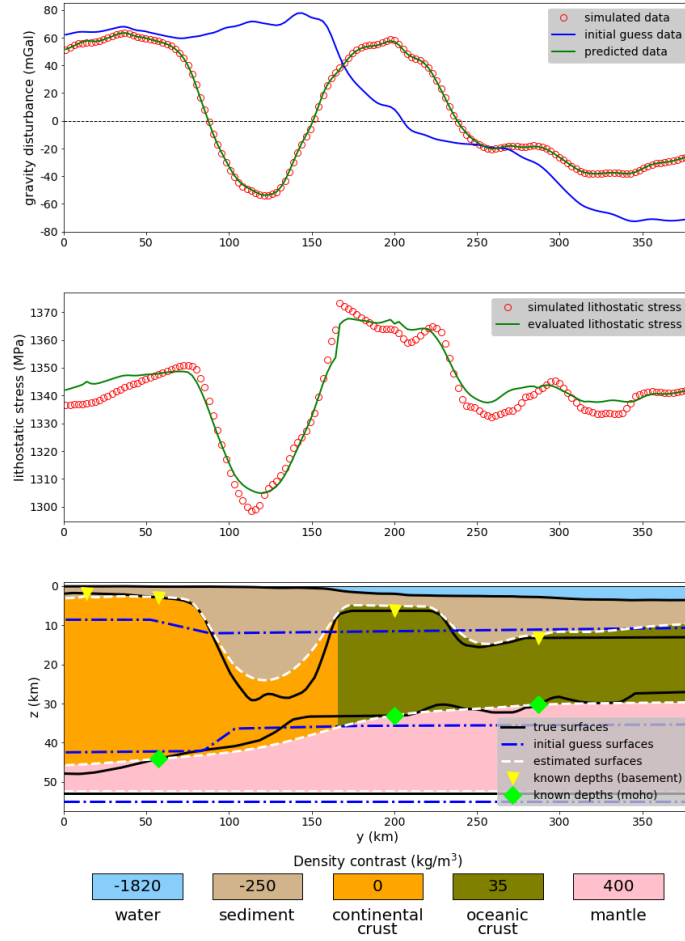


Figure 4: Application to synthetic data. Results obtained at Step 1. (Bottom panel) True and estimated surfaces, initial basement and Moho used in the inversion (initial guess) and a priori information at some points on basement and Moho (known depths). (Middle panel) True and predicted lithostatic stress curves computed by using equation 6. The values are multiplied by a constant gravity value equal to  $9.81 \text{ m/s}^2$ . (Upper panel) Gravity disturbance data produced by the volcanic margin model (simulated data), by the estimated model (predicted data) and by the initial guess (initial guess data). Parameters  $\tilde{\mu}_1$ ,  $\tilde{\mu}_2$  and  $\tilde{\mu}_3$  (equation 22) have values  $10^1$ ,  $10^1$  and  $10^2$ , respectively,  $S_0 = 48 \text{ km}$  and the density contrasts are those shown in Table 1.

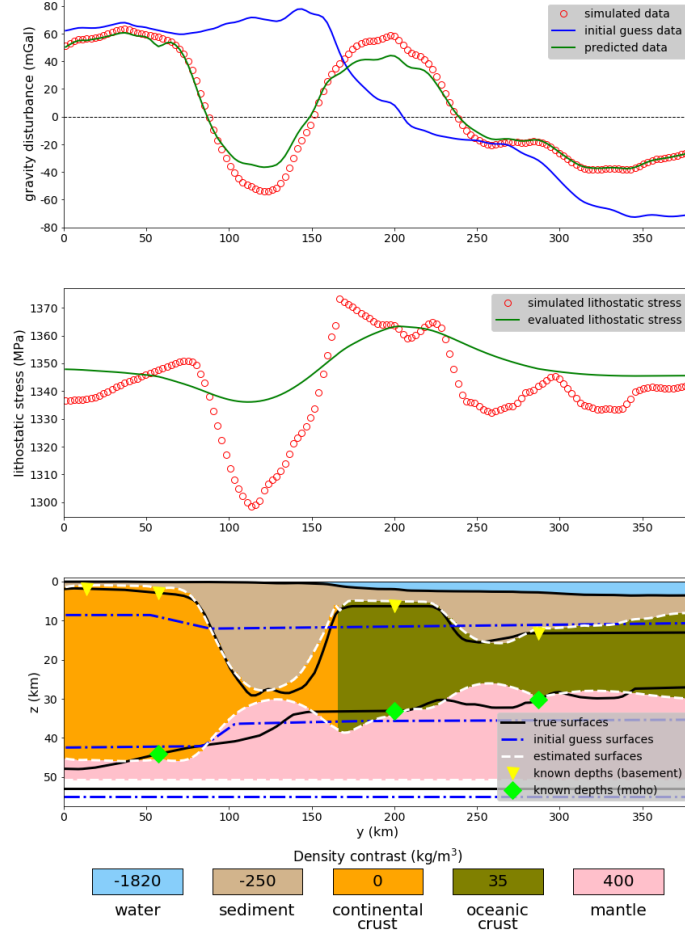


Figure 5: Application to synthetic data. Results obtained at Step 2 by using  $\tilde{\mu}_0 = 10^3$  (equation 22). The remaining informations are the same shown in the caption of Figure 4.

– GEO-XXXX



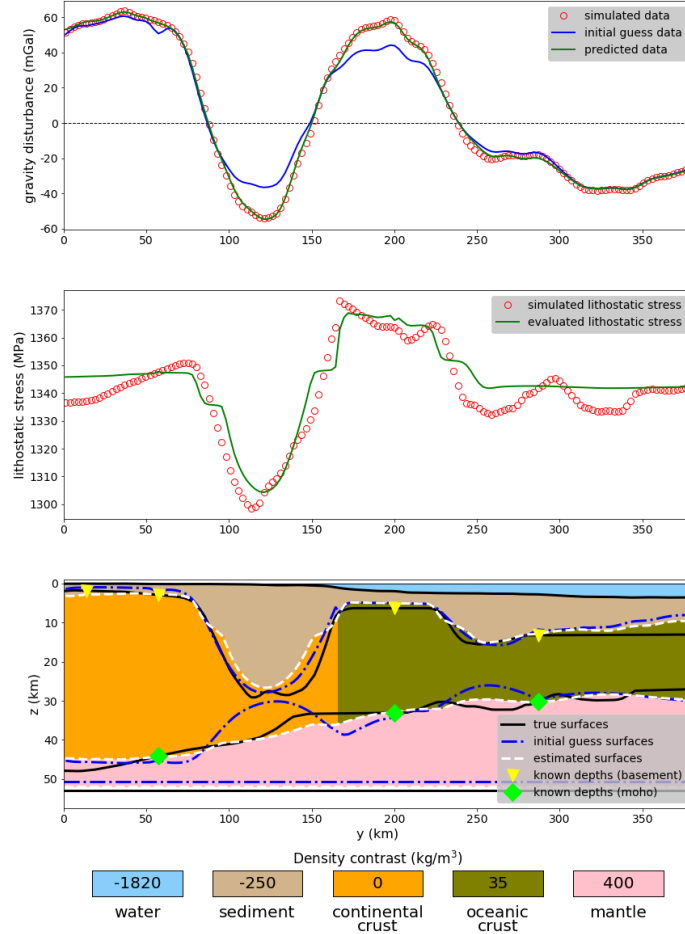


Figure 6: Application to synthetic data. Results obtained at Step 3 by using the estimated model shown in Figure 5 as initial approximation (dashed blue lines) and  $\sigma = 11$  (equation 23). The remaining informations are the same shown in the caption of Figure 4.

– GEO-XXXX

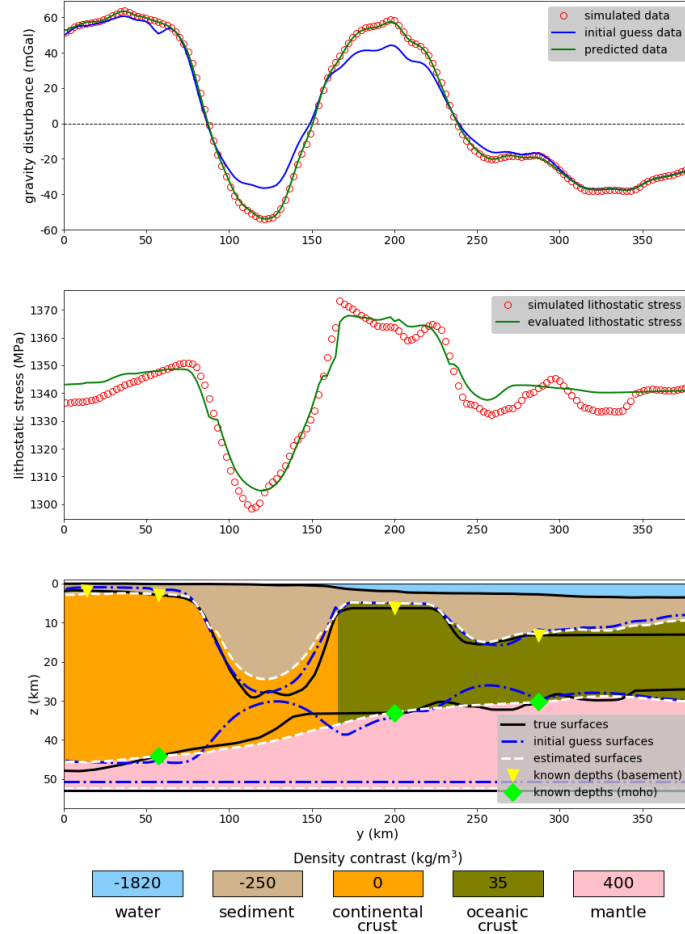


Figure 7: Application to synthetic data. Results obtained at Step 3 by using the estimated model shown in Figure 5 as initial approximation (dashed blue lines) and  $\sigma = 1$  (equation 23). The remaining informations are the same shown in the caption of Figure 4.

– GEO-XXXX

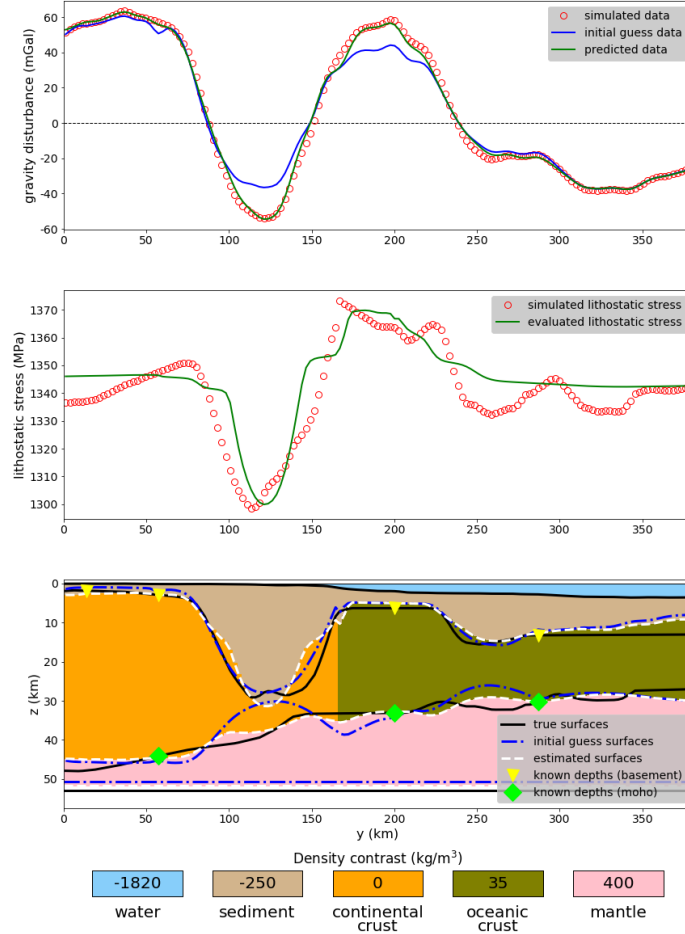


Figure 8: Application to synthetic data. Results obtained at Step 3 by using the estimated model shown in Figure 5 as initial approximation (dashed blue lines) and  $\sigma = 18$  (equation 23). The remaining informations are the same shown in the caption of Figure 4.

– GEO-XXXX

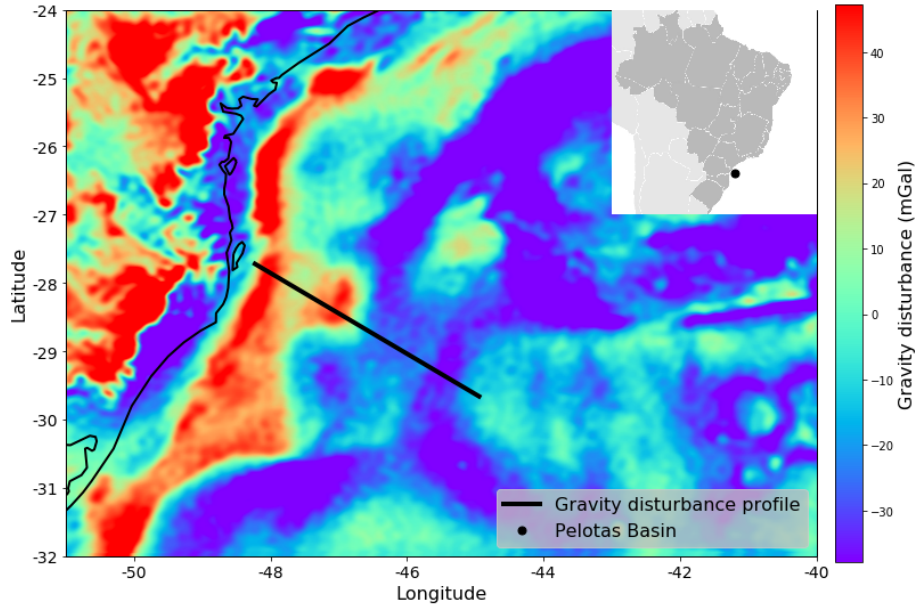


Figure 9: Application to real data on Pelotas basin, Brazil. Gravity disturbance provided by the global gravity field model EIGEN-6C4 (Förste et al., 2014) at the study area. The black straight line indicates the gravity profile over the Pelotas basin. The end points of the profile have coordinates (geodetic latitude and longitude)  $(-27.72, -48.23)$  and  $(-29.66, -44.94)$ . The coordinates are referred to the WGS84 datum.

– **GEO-XXXX**

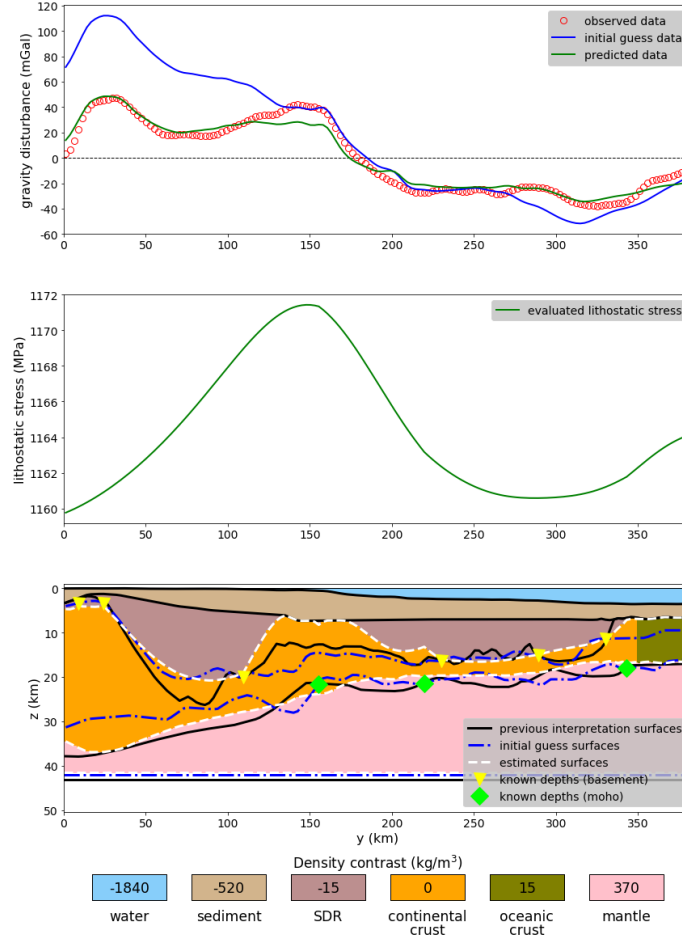


Figure 10: Application to real data on Pelotas basin, Brazil. Results obtained at Step 2.

(Bottom panel) Estimated surfaces, initial basement and Moho used in the inversion (initial guess) and a priori information at some points on basement and Moho (known depths).

The continuous black lines represent a previous interpretation presented by Zalán (2015) at the same study area.

(Middle panel) Estimated lithostatic stress curve computed by using

equation 6. The values are multiplied by  $9.81 \text{ m/s}^2$ .

(Upper panel) Observed gravity disturbance, data produced by the estimated model (predicted data) and data produced the by

the initial approximation (initial guess data). We used  $(\tilde{\mu}_0, \tilde{\mu}_1, \tilde{\mu}_2, \tilde{\mu}_3) = (10^2, 10^1, 10^1, 10^2)$

(equation 22),  $S_0 = 41 \text{ km}$ , density contrasts equal to those shown in Table 1 and initial

approximation for  $\Delta S$  equal to 1 km.

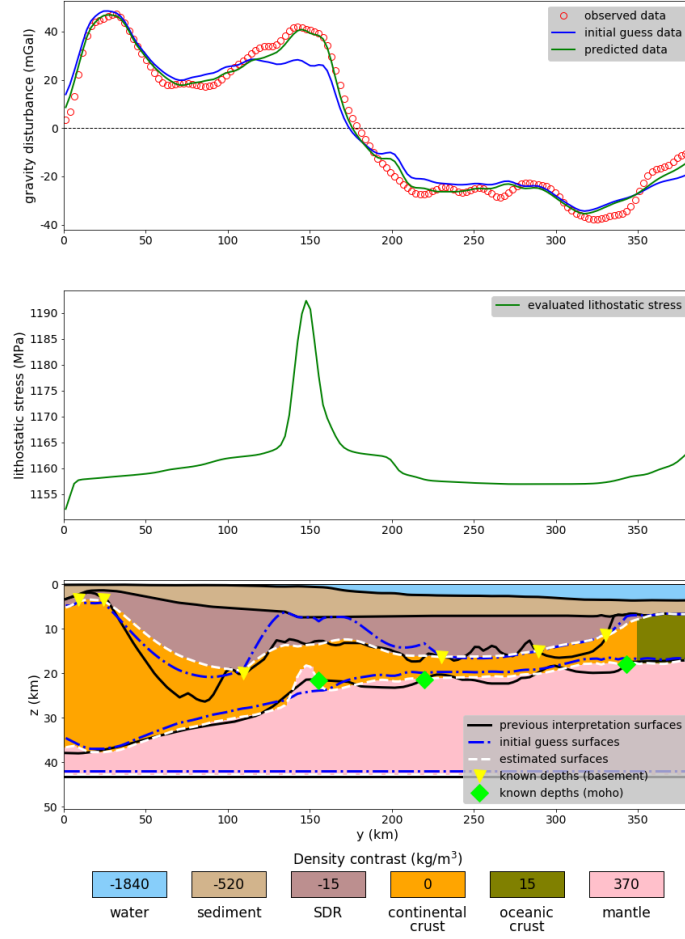


Figure 11: Application to real data on Pelotas basin, Brazil. Results obtained at Step 3 by using the estimated model shown in Figure 10 as initial approximation (dashed blue lines) and  $\sigma = 58$  (equation 23). The remaining informations are the same shown in the caption of Figure 10.

– **GEO-XXXX**

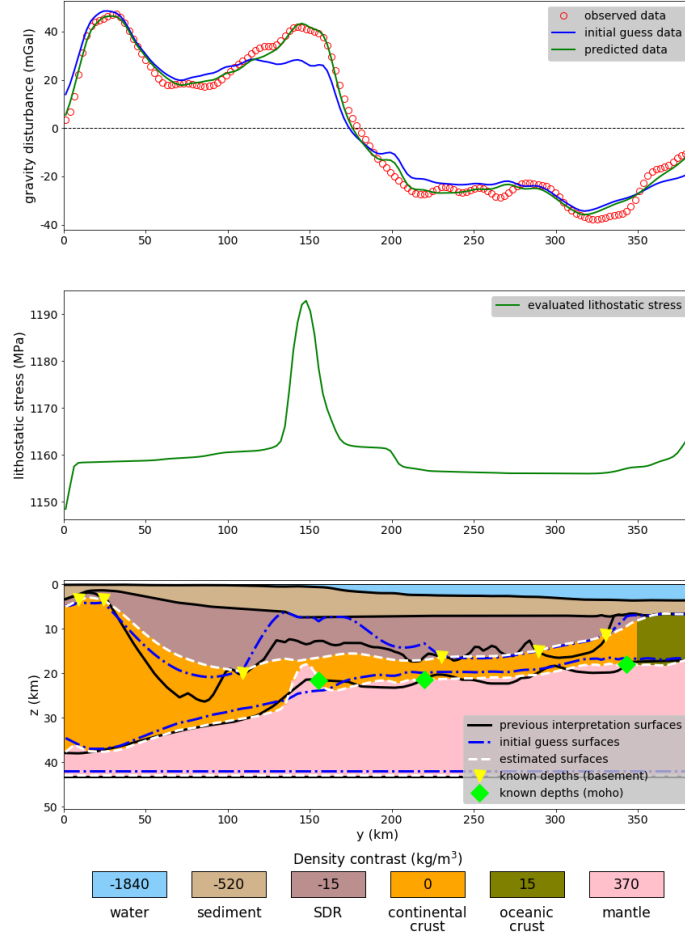


Figure 12: Application to real data on Pelotas basin, Brazil. Results obtained at Step 3 by using the estimated model shown in Figure 10 as initial approximation (dashed blue lines) and  $\sigma = 40$  (equation 23). The remaining informations are the same shown in the caption of Figure 10.

– **GEO-XXXX**

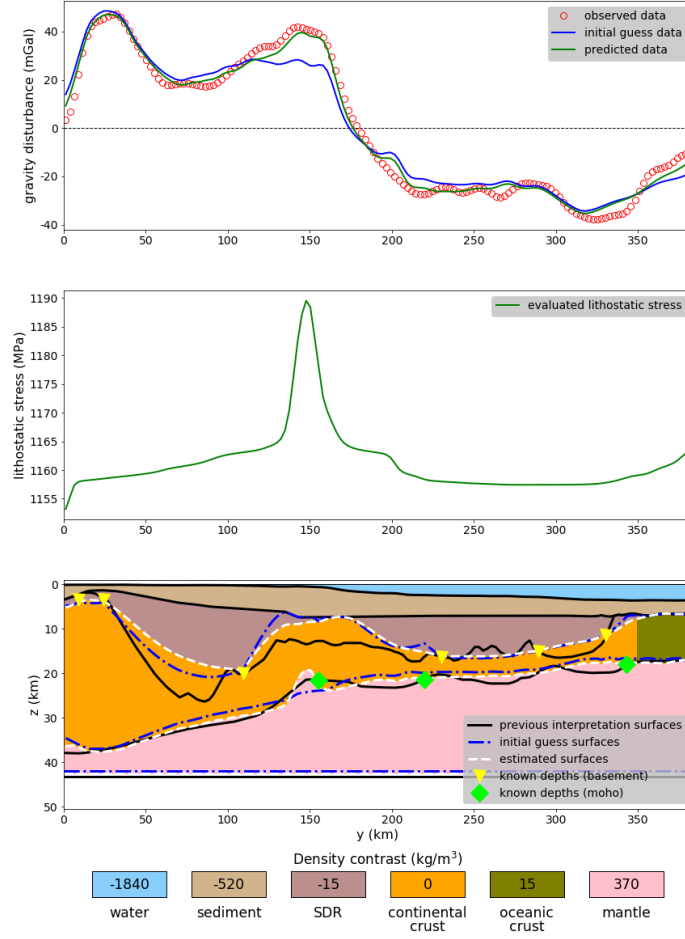


Figure 13: Application to real data on Pelotas basin, Brazil. Results obtained at Step 3 by using the estimated model shown in Figure 10 as initial approximation (dashed blue lines) and  $\sigma = 63$  (equation 23). The remaining informations are the same shown in the caption of Figure 10.

– **GEO-XXXX**



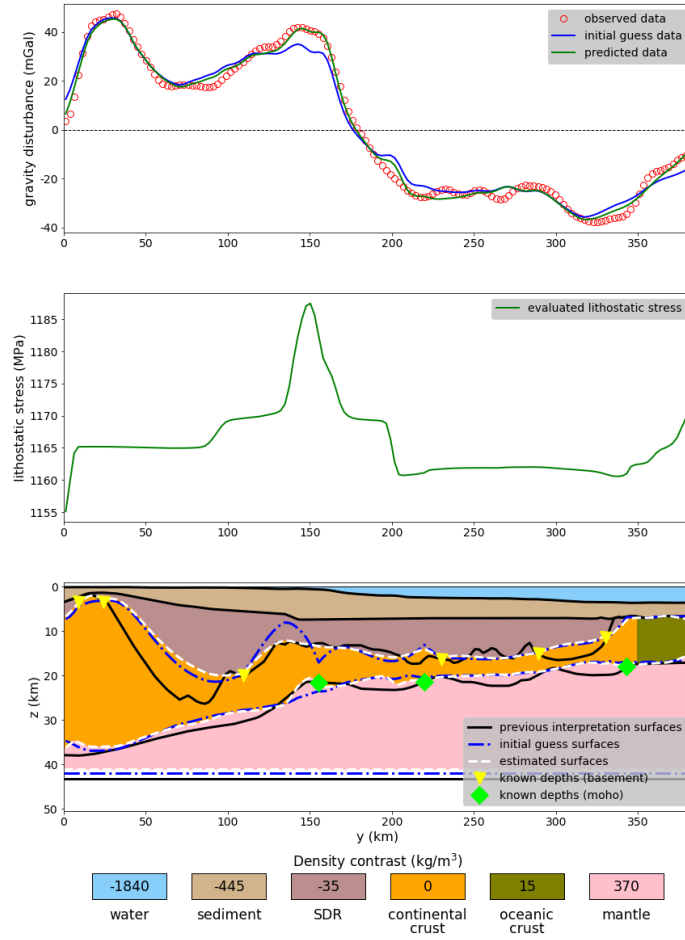


Figure 14: Application to real data on Pelotas basin, Brazil. Results obtained at Step 3 by using density values  $\rho^{(1)}$  (sediment) and  $\rho^{(2)}$  (SDR) different from those defined in Table 1. This estimated model was obtained by using  $\sigma = 17$  (equation 23). The dashed blue lines (initial guess surfaces) represent the corresponding model obtained at Step 2 (not shown). The remaining informations are the same shown in the caption of Figure 10.

– GEO-XXXX